The extreme forest fires in California/Oregon in 2020: Aerosol optical and physical properties and comparisons of aged versus fresh smoke

Q1 Q5

Thomas F. Eck[a,b,*], thomas.f.eck@nasa.gov, Brent N. Holben[b], Jeffrey S. Reid[c], Alexander Sinyuk[b,d], David M. Giles[b,d], Antti Arola[e], Ilya Slutsker[b,d], Joel S. Schafer[b,d], Mikhail G. Sorokin[b,d], Alexander Smirnov[b,d], Anthony D.

Q2
LaRosa[b,d], Jason Kraft[b,f], Elizabeth A. Reid[c], Norman T. O'Neill[g], E.J. Welton[b], Arsenio R. Menendez[b,d]

[a]University of Maryland Baltimore County, Baltimore, MD, USA

[b]NASA/GSFC, Greenbelt, MD, USA

[c]US Naval Research Laboratory, Monterey, CA, USA

[d]Science Systems Applications, Inc., Lanham, MD, USA

[e]Finnish Meteorological Institute, Kuopio, Finland

[f]Fibertek Inc., Herndon, VA, USA

[g]Centre d'Applications et de Recherches en Télédétection (CARTEL), Université de Sherbrooke, Sherbrooke, Quebec, Canada

[*]Corresponding author. Code 618, NASA/Goddard Space Flight Center, Greenbelt, MD, 20771, USA.

Abstract

Wildfire activity in the western United States during August to October 2020 was exceptional in terms of the fire severity and area burned. Extremely dry biomass fuels from near historic multi-year drought conditions were further exacerbated with very hot and dry conditions in 2020. These conditions when coupled with strong offshore flow allowed many ignitions to grow into extremely large and severe wildfires. Long-term monitoring at a few AERONET sites in California showed that the number of days with high Aerosol Optical Depth at 440 nm ($AOD_{440}>1$) in 2020 was greater than any other year going back to the beginning of the data records in 2002. A wide range of fine mode particle volume median radii were retrieved from AERONET data over the course of these fires suggesting significant variability in combustion conditions and aging processes. Additionally, the fine mode radii in some of these smoke plumes in 2020 were very large especially at high AOD ($\sim$0.22–0.32 μm volume median radius), likely due to both coagulation and condensation occurring during aging at very high particulate concentrations. The largest fine mode particle radii combined with narrow distributions resulted in some very rare AOD spectra showing peak AOD at 500 nm and decreasing to lower AOD at both shorter and longer wavelengths. The most extreme retrieved size distributions and associated measured AOD spectra were principally observed in long-distance transported smoke plumes from these western United States fires at sites in Colorado, Maryland and Virginia, possibly due to further aging during transport. Additionally, strong absorption was sometimes observed at short wavelengths with much lower single scattering albedo at 440 nm compared to 675 nm in some plumes consistent with significant brown carbon (BrC) and/or coated black carbon (BC) absorption in biomass burning particles. This strong spectral absorption signature observed at some California sites and dates remained similarly strong in some smoke plumes observed at some east coast sites

in Maryland and Virginia, thereby suggesting that the lifetime of these particular BrC and/or coated BC absorbing species was greater than 5 days.

Data availability

Data will be made available on request.

1 Introduction

Wildfire frequency, size and duration in the western United States (US) have all rapidly increased in recent decades (Iglesias et al., 2022), along with significant increases in associated hazards to health and the environment. Westerling et al. (2006) analyzed large fire frequency in the western US from 1970 to 2003 and found that the area burned since the mid 1980s increased by a factor of 6.5 times relative to the earlier years. This was attributed primarily to higher temperatures leading to earlier snowmelt and thereby drier forest conditions. They also found a significant increase in the length of the fire season plus longer burn duration of the average large wildfire. Abatzoglou and Park Williams (2016) later estimated that anthropogenically caused climate change has resulted in a near doubling of forested area burned in the western US over the 1985 to 2015 interval. They consistently concluded that increasing fire activity is due to higher temperatures and drier conditions resulting in high levels of measured biomass fuel aridity. In addition to increases in annual area burned in recent years due to a shift towards hotter and dryer conditions in the western US, the amount of area burned by high severity fires has also increased significantly, by a factor of eight in a 32-year interval (Parks and Abatzoglou, 2020). In addition to earlier snowmelt and earlier dry conditions in western forests, there has also been a trend in California of later onset of the rainy season (Luković et al., 2021) thereby shortening the fall-winter rainy season which results in increased California wildfire risk in the fall season (Swain, 2021; Goss et al., 2020). Such trends appear to be continuing, with 2020 punctuating weather, fuel and fire hazards with record setting atmospheric dryness in the western US as quantified by the vapor pressure deficit partly due to associated low levels of fuel moisture content-a parameter that has been well correlated with burned area (Higuera and Abatzoglou, 2021).

Increases in western US wildfires in recent decades have significant impacts for the region, including loss of property and human life as well as extreme health hazards to millions of people from the inhalation of particulates and other components of the biomass burning smoke (Reid et al., 2016). Fine mode particulate mass with diameters less than 2.5 μm ($PM_{2.5}$) has long been known to be the major component of air pollution that adversely affects human health (Dominici et al., 2006; Heo et al., 2014). Recent research by Aguilera et al. (2021) presents epidemiological/statistical evidence that $PM_{2.5}$ in wildfire smoke in California is much more toxic than $PM_{2.5}$ that results from other sources, such as typically from fossil fuel combustion, industrial and natural processes. This may be due to much higher concentrations of certain physiologically harmful chemical species such as polycyclic aromatic hydrocarbons (Wegesser et al., 2009) and reactive oxygen species (Franzi et al., 2011) in biomass burning smoke although the large range in biomass fuel types and combustion temperatures very likely results in significant variability in particle chemistry. Furthermore, data analysis from California, Oregon and Washington in the year 2020 strongly suggests increased incidence of COVID-19 cases and deaths associated with higher wildfire smoke $PM_{2.5}$ levels (Zhou et al., 2021). Clearly, very high concentrations of smoke from wildfires are particularly damaging to human health. Analysis from the

2020 fires in the west also suggest that birds were severely impacted by the widespread smoke in the region resulting in massive bird die-offs (Yang et al., 2021). However hot and arid conditions likely resulted in significant decreases in insect populations thereby adding another related severe stress to birds in the region. Increases in high intensity fires also poses threats to old growth forest ecosystems and the species dependent upon them (Jones et al., 2016). These old-growth forests are also particularly effective in carbon sequestration therefore these fires may result in a damaging positive feedback factor for climate change. The Castle Fire in August 2020 in California was estimated to have killed ~10%–14% of all the large (trunk diameters of 4 feet or more) Giant Sequoia trees on earth (Stephenson et al., 2021; Shive et al., 2022).

In addition to the health effects of particulate matter in smoke it is important to understand the optical and physical properties of biomass burning smoke for their effects on atmospheric radiative forcing (Hansen et al., 1997) and for satellite remote sensing of particulate concentrations in the total column and at the surface (i.e. $PM_{2.5}$). Data obtained from globally distributed AERONET sites have characterized biomass burning aerosol optical and physical properties during other events with extremely high particulate concentrations and very high AOD. Smoke from fires in the boreal region of central Alaska in the major burning years of 2004 and 2005 (Eck et al., 2009) included significant amounts of peat burning in addition to above ground biomass in the forests (Turquety et al., 2007). During the major 2015 biomass burning season in Indonesia the AOD was the highest ever recorded by AERONET for a sustained event of greater than a month (Eck et al., 2019). The fuel type burned in Indonesia in 2015 was predominantly peat and the atmospheric emissions were estimated to have exceeded 80% from peat combustion by three independent types of methodologies (Kaiser et al., 2016; Wiggins et al., 2018; Eck et al., 2019). Smoke from both the Alaska and Indonesia fires during these high AOD years exhibited retrieved AERONET size distributions that had some cases of very large fine mode particle radii (>0.25 μm volume median radius) perhaps from a combination of the fuel type, phase of combustion (smoldering peat) and aging processes such as coagulation and condensation. Retrieved size distributions from these extreme biomass burning events are compared to aged and transported smoke from the CA/OR fires of 2020 in this current study. Additionally it is noted that there is recent and continuing research into the retrieval of AOD from satellite for extremely high AOD events. These extreme events present some challenges in cloud screening and in specification of assumed aerosol properties such as particle size and absorption (Shi et al., 2019, 2021; Gumber et al., 2022).

Reid et al. (2005) provided a literature review of the range in measured aerosol size distributions for various types of biomass burning fuels and associated extent of aging. They showed a very wide range in fine mode particle diameter of greater than a factor of 2, ranging from the smallest for fresh smoke in southern Africa and Brazil of 0.14 μm count median diameter to 0.21 μm for 2–3 day aged smoke in the same locations, to 0.34 μm for aged smoke that originated in Canada and was transported to Europe (all data from the same instrument type - Optical Particle Counters). This estimated 6–7 day aged smoke in Europe which was measured by Fiebig et al. (2003) also had the narrowest measured fine mode width at 1.35 geometric standard deviation as compared to 1.82 for the one-day old Brazil smoke and 1.55 for the 2–3 day old Brazil smoke.

O'Neill et al. (2002; 2005) found from AERONET retrievals and AOD spectra retrievals that boreal forest fire smoke optical properties changed with aging and distance from fire sources, with Angstrom Exponent (dominated by fine mode) decreasing with increasing distance from the source implying larger radius fine particles with aging. Colarco et al. (2004) studied the long-range transport of aerosol from major boreal forest fires in Quebec in early July 2002. They found that modeling particle coagulation over the ~2.5 days of transport in the dense smoke plume resulted in simulated size distributions that were a close match to retrieved size distributions from AERONET at a site in Maryland (Goddard Space Flight Center - GSFC) that was ~1600 km south of the fire locations. Theoretical simulations by Hodshire et al. (2019) of smoke aerosol aging of large slowly diluting plumes yielded increased diameter of particles in combination with narrower width of the size distribution due to coagulation, plus additional increases in diameter from secondary organic aerosol condensation. The cross-continental transport of biomass burning smoke from these CA/OR fires in 2020 provides an opportunity to observe smoke properties from before and after ~3–7 days of transport and aging from measurements and retrievals made at several AERONET monitoring stations.

The absorption properties of biomass burning smoke also vary significantly between different biomass burning regions partly due to variations in fuel types such as forests, savanna and peat (Dubovik et al., 2002, Giles et al., 2012; Eck et al. (2019)). The phase of combustion, either flaming or smoldering, of these biomass fuels varies with both fuel type and moisture content in addition to several meteorological factors including temperature, relative humidity (RH), wind

speed and precipitation. Black carbon (BC) is the principal absorber in biomass burning particles in the mid-visible and near infrared wavelengths and is primarily produced in the flaming phase of combustion. This accounts for the low single scattering albedo (SSA) retrieved by AERONET in savanna regions of Zambia (Eck et al., 2003; Eck et al., 2013) where smoke from savanna grass and shrub burning has a significant percentage of flaming phase to total combustion, as contrasted to the very weak absorption and high SSA for peat combustion in Indonesia due to predominantly smoldering phase combustion of sub-surface peat (Pokhrel et al., 2016). Additional spectral variation of absorption in biomass burning aerosols has been observed in the UV and short wavelength visible in both field measurements (Mok et al., 2016) and in laboratory measurements (Lewis et al., 2008; Pokhrel et al., 2017). This additional UV and short wavelength visible absorption can be due to the absorbing component of organic carbon known as brown carbon (BrC) in addition to BC absorption. It is also possible that BC with organic carbon coatings in biomass burning aerosols can also result in stronger short wavelength absorption in the visible and UV even in the absence of BrC absorption. Theoretical calculations made by Wang et al. (2016) and Konovalov et al. (2021) indicated strong absorption at 440 nm relative to 870 nm for coated BC particles with coating thickness of one to two times the BC core radius. Several studies have inferred that the lifetime of BrC in general is often short ranging from ~few hours to ~2 days (Wang et al., 2016; Di Lorenzo et al., 2017; Wong et al., 2019) in comparison to relatively long-lived BC (days to weeks; Bond et al., 2013). However, Wong et al. (2019) suggested that high molecular weight BrC is relatively long lived, persisting for at least 3 days. Additional studies (Wang et al. (2016); Fleming et al. (2020); Konovalov et al. (2022)) have also found BrC can be relatively long-lived. Most aerosol models do not currently account for BrC absorption (Sand et al., 2021) and more information on this category of particle absorption is needed for a full global understanding of the impacts of this absorbing species. The measurements and retrievals from AERONET sites of the optical properties of the smoke from the extreme fires in Sep 2020 in CA/OR provide an opportunity to measure the spectral variation in SSA at relatively high accuracy from high AOD observations both near the sources and also after long distance transport over several days, and thereby infer some information about the longevity of BrC and/or coated BC in some types of biomass burning aerosols.

Since major forest fire burning years in the western US have been occurring in increased frequency, and predicted to increase in the future, a goal of this paper is to examine the aerosol optical properties of the smoke that occurred in 2020 (focus on September) which was the largest burning year (area burned) to date in California (plus with well observed transport events). The large number, size, severity and duration of the many fires that occurred resulted in major smoke plumes that were actually composed of many contributing smaller plumes from several individual fires that may have had different and varying burning conditions during the fire lifetimes and different aging processes affecting the aerosol composition and size. Such variability in aerosol properties both spatially and temporally need to be considered for the satellite retrieval of smoke properties from these most extreme of forest burning episodes. In this study, the examination of aerosol properties from AERONET data during this largest of biomass burning events in 2020 attempts to characterize the range in variability of aerosol optical properties.

2 Instrumentation, data and methodology

2.1 AERONET instruments and measurement of AOD

AERONET's global network utilizes the CIMEL Electronique CE-318 sun-sky radiometer for measurements of AOD and directional sun-sky radiances in its global network. Holben et al. (1998) provides a complete description of instruments and their use. However, a brief synopsis is provided here. The CE-318 automatically tracks the sun to provide AOD and sky radiance for retrievals with a ~1.25° full field of view. There are some minor instrument variations between sites, but in this study the more standard instrument configuration was used with AOD measurements at eight wavelengths (340, 380, 440, 500, 675, 870, 1020, and 1640 nm), plus 940 nm for water vapor. Sampling rates varied by site, with some sites attempting an AOD measurement every 15 min, while most made measurements approximately every 5 min to obtain high temporal resolution data. It takes ~8 s to scan all wavelengths utilizing a motor driven filter wheel to position each filter in front of the detector, repeated three times within a minute, to provide an ensemble mean and information for cloud screening as described below. Ion assisted deposition interference filters were used with full width at half maximum bandpass of 10 nm, except for 25 nm at 1640 nm and for the 340 and 380 nm channels at 2 nm and 4 nm bandpass, respectively. The estimated uncertainty in AERONET measured AOD, due primarily to calibration uncertainty, is ~0.01–0.02 at optical airmass of one for network field instruments (with the highest errors in the UV; Eck et al., 1999). This estimate is consistent with Schmid et al. (1999)

who compared AOD values derived from 4 different solar radiometers (including an AERONET sun-sky radiometer) operating simultaneously together in field conditions and found that the AOD values from 380 to 1020 nm agreed to within 0.015 (root mean squared). More recently, Barreto et al. (2016) found similar results with the latest version of the Cimel. The AOD uncertainty of AERONET reference calibration instruments is significantly better at ~0.002 to ~0.009, again with the higher errors in the UV (Eck et al., 1999) since these instruments are calibrated by the Langley technique at the stable high latitude Mauna Loa Observatory, Hawaii (Shaw, 1983). The uncertainty in the UV is higher due to slightly poorer repeatability of the Langleys Vo's and also due to the narrow bandpass with probable out-of-band energy leakage. Data from the GSFC site reference instrument provide a key set of observations in this current study. The sky radiances are calibrated versus frequently characterized integrating spheres at the NASA Goddard Space Flight Center, assumed to have an absolute accuracy of ~3% (Sinyuk et al., 2020) in Version 3. A map showing the distribution of the principal sites located in the US that were analyzed in this study is given in Fig. 1.

alt-text: Fig. 1

Fig. 1

Map showing the principal AERONET sites in the United States analyzed in more detail in this study. The box shows the region of latitude range 32N–46N longitude range of 114W–125W for which satellite averaged AOD are shown in Fig. 2.

alt-text: Fig. 2

Fig. 2

Time series of the monthly averaged 550 nm AOD from 2000 to 2021 retrieved from the merged Dark Target and Deep Blue algorithms utilizing MODIS instrument data. These monthly averages were computed for the area defined by the latitude range 32N–

46N and longitude range of 114W–125W, which encompasses all of California and Oregon plus portions of neighboring states and part of the coastal Pacific Ocean.

Most analyses presented here utilized level 2 data (post calibrated and cloud screened) from the new Version 3 spectral AOD product described in detail by Giles et al. (2019), however some sites used L1.5 data when L2 were not yet available (final post-deployment calibration not yet made). All of the 2020 data are Level 2 while most of the spectral AOD from 2021 are Level 1.5. AOD uncertainties in Level 1.5 data that do not have the final calibration applied are on average an additional ~0.01 higher at 500 nm at mid-day and mid-deployment (assuming a 1–2 year deployment interval), therefore exhibiting an average uncertainty of ~0.02 at 500 nm (Giles et al., 2019). The complete set of Version 3 cloud screening and quality assurance algorithms are presented and analyzed in Giles et al. (2019).

2.2 AERONET inversion methodology

The almucantar sky radiance scans made by the CIMEL instruments are performed at fixed elevation angles equal to the solar elevation with ±180° azimuthal sweeps made sequentially at seven wavelengths (380, 440, 500, 675, 870, 1020 and 1640 nm). In the standard retrieval product only the data from 440, 675, 870 and 1020 nm are input to the inversion algorithm. In the first decades of the AERONET project the instruments only measured sky radiances at these four wavelengths while AOD were measured at 3-4 additional wavelengths. Later sky radiance measurements were added at 380, 500 and 1640 nm for the newest model instruments but these are not yet incorporated into the operational retrievals and database. All sky scan retrievals in the AERONET Version 3 database were only inverted for these 4 wavelengths since these are the common wavelengths for all instruments and all sites. The almucantar scans are made in both the morning hours and afternoon hours at optical airmasses of 4, 3, 2, and 1.7 (75, 70, 60, 54° solar zenith angle, or SZA, respectively) plus once per hour in between. AERONET retrievals are also made utilizing hybrid sky scans with the new Cimel instruments version Model-T. The sky scan made with the hybrid methodology simultaneously moves in both the azimuthal and zenith angle directions, thus performing a scan that is in general intermediate between the almucantar and principal plane (varies the zenith angle while maintaining a fixed azimuth).

Hybrid and almucantar directional scan radiance data are combined with measured AOD data at identical wavelengths as inputs to retrieve optically equivalent column-integrated volume size distributions and aerosol refractive indices utilizing the algorithms as developed by Dubovik and King (2000) and Dubovik et al. (2006). The Dubovik and King (2000) inversion algorithm in AERONET makes no assumptions about the spectral variation of AOD. The inversion fits the measured AOD to within 0.01 consistent with the measurement accuracy of the direct sun measured AOD, and along with the retrieved size distribution and complex refractive indices computes the radiative transfer calculated sky radiances with residual errors of maximum of 5–8% (larger threshold at higher AOD) of the measured values for Level 2 retrievals. These retrieved aerosol properties are utilized to derive additional parameters such as asymmetry parameter, single scattering albedo, and phase function. The new Version 3 Level 2 retrievals with the quality controls described in Holben et al. (2006) are presented in this study (see Sinyuk et al., 2020 for details). The percentage particles of spheroidal and spherical shape required to give the best fit to the measured angular distribution of spectral sky radiances is also determined by the AERONET retrieval algorithm. Dubovik et al. (2006) provides further details on these retrieval algorithms. Some research level retrievals (preliminary results) are studied that focus on algorithm changes to the retrieval of the imaginary refractive index and also include additional spectral channels as input, these are discussed in more detail below.

In order to ensure sky radiance measurements over a sufficiently wide range of scattering angles in this study, only almucantar scans taken at solar zenith angles greater than ~50° are analyzed and presented. The scattering angle range of measured sky radiances for an almucantar scan performed at 50° SZA is 100° while at 75° SZA it is 150°. However, the newly developed hybrid scans available only with the recent Model-T Cimels can provide directional sky radiance measurements with 100° scattering angle range at a solar zenith angle of only 25°. Additional cloud screening for hybrid and almucantar sky radiance measurements (first the AOD must pass the level 2 quality control and cloud screening) was performed through the requirement of symmetrical sky radiances on both sides of the sun at equal scattering angles. These radiances from both sides of the scan that meet the symmetry threshold are then averaged before being used as input to the AERONET retrieval. Directional sky radiance measurements that are asymmetrical at a given scattering angle (due to inhomogeneous aerosol distributions or cloud on one side) are eliminated, and a retrieval only reaches Level 2 when the minimum number of measurements required in defined scattering angle ranges are met (see Holben et al., 2006). However, the hybrid criterion for the last scattering angle bin has a different minimum

scattering angle limit (≥75°) than almucantars (≥80°) and a different minimum number of symmetric scattering angles (N = 2) than almucantars (N = 3), due to somewhat fewer scattering angle range measurements in the hybrid scan. Dubovik et al. (2000) found these AERONET inversions to be stable as determined by perturbation analyses accounting for random errors, instrumental data offsets and known uncertainties in the atmospheric radiation model. Sinyuk et al. (2020) found excellent agreement between almucantar and hybrid scan retrievals made within 12 min of each other.

Although few direct comparisons of size distributions between AERONET retrievals and in situ measurements have yet been published, there are several specific regional aerosol types that have been compared. For example, for biomass burning aerosols Reid et al. (2005) compared regional mean volume median radii from source regions in southern Africa, South America, boreal zone and temperate North America and found that AERONET retrievals versus in situ measurements of the diameter of fine mode particles were often within ∼0.01 μm of each other. In the Arabian Sea for fine mode pollution particles observed during the INDOEX experiment, Clarke et al. (2002) showed volume size distribution lognormal fits from both aircraft and ship in situ measurements where the average accumulation mode volume peak radius values under high aerosol loading conditions ranged from 0.17 μm to 0.18 μm with corresponding geometric standard deviations (widths) of 1.51 (for ship) and 1.43 (for aircraft). This compares very well to AERONET retrievals made at Kaashidhoo Island in the Maldives (in the INDOEX region), for observations when AOD(440 nm) > 0.4, of median radius of 0.18 μm and width of 1.49 (1998–2000 multi-year average Version 2 values). Recently, Schafer et al. (2019) compared time and location matched in situ measured fine mode size distributions with AERONET retrievals from aircraft profiles at three locations in the US. They found that when the in situ data were corrected for ambient RH conditions the agreement with the remote sensing retrievals was excellent, with fine mode peak radius differences averaging 0.01 μm. For larger sub-micron size aged Pinatubo volcanic stratospheric aerosols, Eck et al. (2010) discussed the relatively close agreement between in situ observations from stratospheric aircraft of 0.53 μm effective radius as reported by Pueschel et al. (1994) to AERONET retrievals made from observations in 1993 of ∼0.56 μm peak volume radius. For coarse mode particles (with super-micron radius), Reid et al. (2006, 2008) found excellent agreement between AERONET retrieved and in situ measured size for sea salt and desert dust aerosol, respectively. For aerosols of maritime origin, Smirnov et al. (2003) showed reasonable agreement between AERONET retrievals and in situ measurements of sea salt dominated coarse mode size distributions. Additionally, for coarse mode dust size distributions in the Sahel region of West Africa Johnson and Osborne (2011) have shown good agreement between AERONET retrievals and in situ measurements from aircraft.

In this study, we followed the guidance from Dubovik et al. (2000) and the V3 database for Level 2 quality control that only almucantar retrievals where 440 nm AOD is greater than 0.4 be used for analysis of spectral refractive indices and single scattering albedo. In southern Africa, for strongly absorbing fine mode dominated biomass burning aerosols, Leahy et al. (2007) found good agreement in 550 nm single scattering albedo, with differences between in situ measurements and AERONET retrievals of −0.01. In the mid-Atlantic region of the United States for weakly absorbing anthropogenic fine mode dominated aerosol, Schafer et al. (2014) found excellent agreement between aircraft vertical profiled in situ measurements of single scattering albedo (550 nm) and AERONET retrieved values (estimated at 550 nm from the mean of 440 and 675 nm values), with an average difference of only ∼0.01 for spatially and temporally matched observations. These offsets are significantly smaller than the nominal ∼0.03 uncertainty of AERONET SSA at AOD(440) of 0.40 (Sinyuk et al. (2020). Additionally Sinyuk et al. (2020) show that the SSA uncertainty decreases as AOD increases. Since most smoke AOD measurements in this paper exceed 1.0 at 440 nm, the SSA retrieval uncertainties ranges from ∼0.02 to ∼0.01 for 440 nm and 675 nm, with somewhat higher uncertainties at 870 nm and 1020 nm.

This paper primarily utilizes the Version 3 AERONET database and data products. All of the V3 retrievals presented for 2020 are level 2 data. However, we do present some Level 1.5 retrievals of fine mode volume median radius of the size distributions for the year 2021 when post deployment calibrations had not yet been performed. Additionally, in Section 3.6 we discuss and present some retrieval results that utilize different constraints on the spectral variation of the imaginary refractive index than were applied in V3, and which are planned to be included in the upcoming Version 4 retrievals and database. These new constraints allow for more spectral variation of imaginary refractive index at the shorter wavelengths than in V3 in order to have improved sensitivity to BrC absorption and/or absorption of coated BC particles and to enable a better fit of the measured to computed sky radiances at these wavelengths. Detailed discussion and comparisons of these new retrievals with relaxed constraints of the spectral imaginary refractive index are given in

Sinyuk et al. (2022). Additionally some of these new retrievals are made with more spectral input data than the standard four channels of 440, 675, 870 and 1020 nm, adding the 380 nm and 500 nm sky radiances and AOD to enable a six channel retrieval. The addition of the 380 nm data to the retrieval in particular provides enhanced sensitivity to the stronger BrC and/or coated BC absorption in the shorter wavelengths (Mok et al., 2016; Wang et al., 2016). The 380 nm sky radiances need to be calibrated using a different methodology however since the standard integrating sphere does not provide sufficient radiance output at this wavelength. Therefore a vicarious technique (Li et al., 2008) has been applied in order to compute the calibration for this channel for this paper, while several options for 380 nm radiance calibration are being considered for the upcoming V4 data processing. Since the calibration procedures and estimated uncertainty for the 380 nm channel are not yet finalized, these results should be considered as preliminary.

2.3 Auxiliary satellite and lidar data sets

In order to understand the nature of smoke emission and transport for our study period we utilized many of the online datasets and visualization tools designed specifically to this purpose. Satellite visualization for Terra and Aqua MODIS and NOAA-20 VIIRS was provided by NASA Worldview (https://worldview.earthdata.nasa.gov/; last accessed 22MAR2023). For meteorological model overlays, these were added using the Navy Global Environmental Model (*NAVGEM; Hogan* et al., *2014*) available on the Global Oceans Data Assimilation Experiment Archive (https://usgodae.org; last accessed 22MAR2023). Back trajectories from the GSFC site were calculated from the Hybrid Single-Particle Lagrangian Integrated Trajectory model (HYSPLIT; Stein et al., 2015). MODIS and VIIRS AOD data was drawn from daily Combined Dark Target/Deep Blue product (Sayer et al., 2014; Levy et al., 2013) generated by the NASA GIOVANNI server (https://giovanni.gsfc.nasa.gov/giovanni/; last accessed 22MAR2023). Finally, lidar plots from CALIPSO and MPLNet are drawn from their browse servers at (https://www-calipso.larc.nasa.gov/products/lidar/browse_images/exp_index.php; last accessed 22MAR2023) and (https://mplnet.gsfc.nasa.gov/; last accessed 22MAR2023), respectively.

3 Results

3.1 Comparison of 2020 burning season to long-term monitoring on the west coast and California

In order to derive plume extent over all land surface types in the region, we first analyzed the MODIS combined Dark Target/Deep Blue retrievals of AOD for California, Oregon, Nevada, parts of Idaho, and associated coastal ocean using both the Terra and Aqua satellites (Sayer et al., 2014). Monthly averaged Level 3 data (MOD08; King et al., 2003) of the 550 nm AOD retrievals were utilized for all data from 2000 through 2021 for the latitude-longitude region of 32–46° N and 114–125° W, see inset box in Fig. 1. The box limits in Fig. 1 were selected to encompass all of California and Oregon which were the locations for the major intense wildfires that occurred in September 2020. This defined area provides a wider geographic context of the extent and magnitude of the smoke AOD that a single or even multiple AERONET sites can provide. The time series plot of the monthly mean AOD data for this region is shown in Fig. 2. There is a repeating annual cycle of highest AOD in the summer and lowest in the winter, primarily due to the higher AOD smoke during the biomass burning seasons in the summer and fall months. The years 2020 and 2021 clearly stand out as having the highest monthly average AOD of the entire record, with the highest value in September 2020 and the second highest in August 2021. The next highest monthly average AOD values in descending order occurred in August 2018, July 2008, and September 2017. For this 22-year data record nearly all of the highest AOD years occurred during the summer-fall biomass burning months from 2017 to 2021, with only the relatively cool and wet year of 2019 having lower than average summer AOD in that interval. The smoke AOD was so high in early to mid-September 2020 that the thickest AOD was not retrieved by the operational MODIS Dark Target and Deep Blue algorithms, therefore the September 2020 estimate in Fig. 2 is certainly an underestimate. However similar underestimates may have also occurred in other years. Currently special research level satellite retrievals are required to retrieve the AOD as such high levels (e.g. Shi et al., 2019).

We next examined long period monitoring data at three AERONET sites in California in this section in order to investigate in more specific detail the 2020 biomass burning season on a site-by-site basis (sites noted in Fig. 1). Long-term multi-year monitoring of AOD at Table Mountain CA, Fresno (two sites ~0.4 km apart) and Monterey sites all show that 2020 was a year with exceptionally high AOD resulting from the extreme intensity and number of wildfires in August and especially September through early October of 2020. AERONET monitoring began in 2002 at the Fresno and Monterey sites and in 2004 at the Table Mountain site. These three AERONET stations are the ones in CA

that have the best long-term data records without significant data gaps in AERONET Level 2 data over almost 20 years of monitoring. At the Fresno site the number of days when daily average Level 2 AOD at 440 nm exceeded 1 in 2020 was 24 days while the next highest year was 2021 with 11 days and the third highest was 2018 with only 4 days exceeding AOD(440) of 1 (see Fig. 3a). At the Table Mountain, CA site at an altitude of 2200 m the AOD was much lower since much of the smoke was lower than the altitude of this mountaintop-instrumented site plus this site is ~250 km further south than Fresno. AERONET monitoring at Table Mountain, CA in 2020 ceased for that calendar year on September 29, 2020 so no data were available after that date in 2020. However 2020 was also a year of exceptionally high AOD at this site with 15 days of daily average Level 2 AOD (440 nm) greater than 0.3 (maximum of 1.95 on Sep 7, 2020) compared to the second highest year of 2021 at 7 days while the next highest AOD years (7 different years) all had only 1 day with AOD exceeding 0.3 (Fig. 3b). At the Monterey site the year 2020 also had the most days with AOD exceeding 1.0 at 440 nm with 14 days compared with 5 days in 2021, 6 days in 2016 and 8 days in 2008 (Fig. 3c). The Monterey site experienced more high level AOD days in 2008 and 2016 than the other two sites possibly because it is located to the west of the other sites and therefore more likely to be affected by smoke plumes advected from fires in the coastal mountain ranges. Other meteorological factors involving upwind source locations and advection and stagnation of smoke plumes may have also been factors in higher smoke levels at Monterey in 2008 and 2016. Under extremely high AOD conditions the AOD cannot be measured since the high value limit of sun photometry in measuring AOD is AOD*m < 7.3 where m is the optical airmass or path length through the atmosphere (Eck et al., 2019; Sinyuk et al., 2012; Giles et al., 2019). Typical values of m ranged from 1.15 to 7 in September 2020 (solar noon lowest while the beginning and end of day maximum m is set to 7 in the AERONET database). There were no missing days of L2 AOD at the Fresno and Table Mountain sites in 2020 therefore it seems that this limit which is applied on an individual measurement basis may not have had a large effect on the daily average data. Nonetheless it is likely that there was some missing data at AOD levels too high to measure by sun photometer but the magnitude of the impact of this missing data is unknown. At another location, at the NASA Ames AERONET site on September 9, 2020 all wavelengths except for 1020 and 1640 nm were attenuated and there were only three instantaneous measurements that included both of these wavelengths for that entire day at that location. The Angstrom Exponent computed from the 1020 and 1640 nm AOD for this case was 2.2 therefore clearly dominated by fine mode sized particles. Two days later at the same site some 440 nm AOD values were measured so that the 440–1020 nm two wavelength Angstrom exponent could be computed, to yield an average value of 1.30. Using this Angstrom exponent (440–1020 nm) for the Sep 9, 2020 measured 1020 nm AOD value of 5.4 at the NASA Ames site it was estimated that the 440 nm AOD was ~14–~19 assuming an uncertainty of 0.2 in the applied 440–1020 nm Å (assumed AE range of 1.10–1.50). It is very likely however that the AOD exceeded even these values since there were only three measurements at the longest wavelengths at this site and date, therefore it is likely that nearly complete attenuation of the solar direct beam from smoke aerosols occurred even at these wavelengths sometime during that particular day.

Images are optimised for fast web viewing. Click on the image to view the original version.

alt-text: Fig. 3

Fig. 3
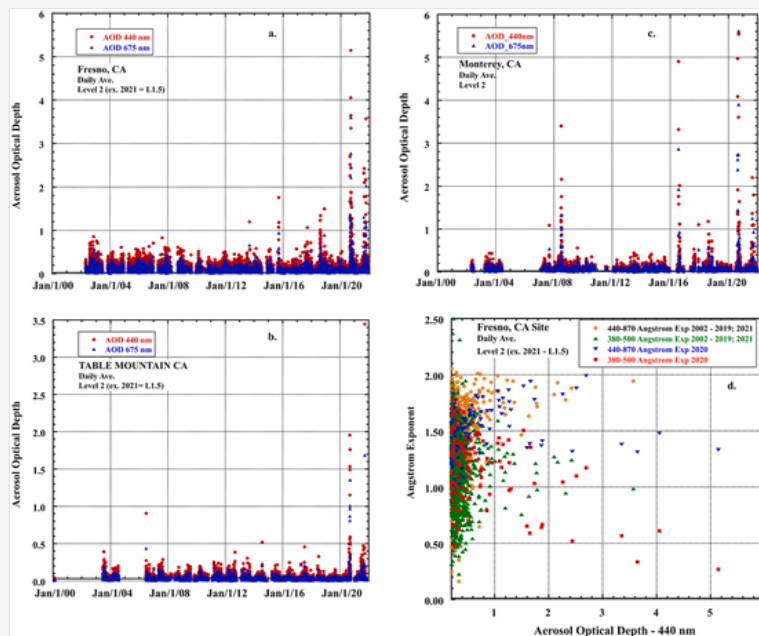
(a) Time series of daily average AOD (440 and 675 nm) measured at the Fresno & Fresno 2 AERONET sites (~0.4 km apart; altitude 100 m) in the Central Valley of California. All data are Level 2 except for 2021. (b) Similar to (a) but for the Table Mountain CA AERONET site at 2200 m altitude which is a primary factor in the lower AOD levels compared to Fresno. (c) Similar to (a) but for the Monterey AERONET site except all data are Level 2. (d) Angstrom Exponents (AE) versus AOD (440 nm) for the Fresno AERONET sites. Spectral values of AE(440–870 nm) and also AE(380–500 nm) are shown for the year 2020 separately in addition to all other years combined.

The daily average of Angstrom Exponent (AE) for two different wavelength ranges at the Fresno site is shown in Fig. 3d. These AE values are computed by linear regression with all of the wavelength data between the two endpoint wavelengths. The AE(440–870) is therefore computed with 440, 500, 670 and 870 nm AOD as it is in most of the rest of the paper unless otherwise noted. The 440–870 nm AE is significantly greater than the 380–500 nm value due to the domination of fine mode size particles and the relatively large radius of these fine particles (Reid et al., 1999; Eck et al., 1999). Focusing on the high aerosol optical depth days where AOD(440)>1 there are several days where the AE(440–870)<1.5 which are relatively low values for biomass burning at least compared to peak burning season values in the southern Amazonia region with a mean of ~1.75 (Schafer et al., 2008) and in southern Africa treed savanna that had a mean AE of ~1.85 (Eck et al., 2013). The AE (380–500 nm) are particularly low in 2020 at very high levels of AOD, suggesting large fine mode particle size (Reid et al., 1999; Eck et al., 1999). The AE provides only general and basic information on aerosol size of both modes combined, therefore we next show more robust and quantifiable data on the smoke particle radius of the fine mode only. The fine mode volume median radius at the Fresno site retrieved from inversions of AOD spectra plus almucantar and hybrid sky radius scans is shown in Fig. 4a. These are all instantaneous values, not daily averages, since significantly fewer sky radiance scans meet the cloud screening requirements as compared to AOD measurements which only require the direct sun to be unobscured by clouds. The fine mode radius for AOD at 440 nm exceeding 0.8 in 2020 show a trend of increasing radii as AOD increased. This is likely due in part to increasing rates of coagulation and condensation as concentration increased in these extremely high AOD conditions (Hodshire et al., 2019) in the heavy smoke plumes which resulted from the many extremely large and severe fires in 2020. For the retrievals with AOD (440) > 1 other than occurred in 2020, there are only ten that are not from the year 2021. The fine mode radii at Fresno in 2021 were significantly smaller than in 2020 at the highest AOD levels, suggesting some differences in the combination of combustion factors, particle aging and meteorological factors between years despite 2020 and 2021 being the record and next highest CA acreage burning years, respectively. Even though the data for this site for the year 2021 is only Level 1.5 (without post-deployment calibration) the accuracy of the retrieved fine mode particle size is very robust with small uncertainty of <0.005 μm for fine mode dominated aerosol at high AOD (Sinyuk et al., 2020) in L2 data and not very sensitive to calibration. The same is not true for retrievals of SSA, and therefore we do not present extensive SSA retrievals from L1.5 data, with the exception of individual cases with very high AOD that reduces the uncertainty significantly. Retrievals of SSA are analyzed in detail in section 3.6. It is also shown in Fig. 4a at Fresno that there were many observations of large fine mode radius for somewhat lower AOD(440)<0.8 for all years, some with very large radius exceeding 0.35 μm. This is partly due to fog processing of pollution aerosols in the San Joaquin Valley in winter when fog occurs relatively frequently. Eck et al.

(2012) showed the seasonal cycle of larger fine mode radius in winter at the Fresno site which was very similar to the seasonal cycle of low cloud fraction (which includes fog) from the MODIS cloud retrievals.

alt-text: Fig. 4

Fig. 4
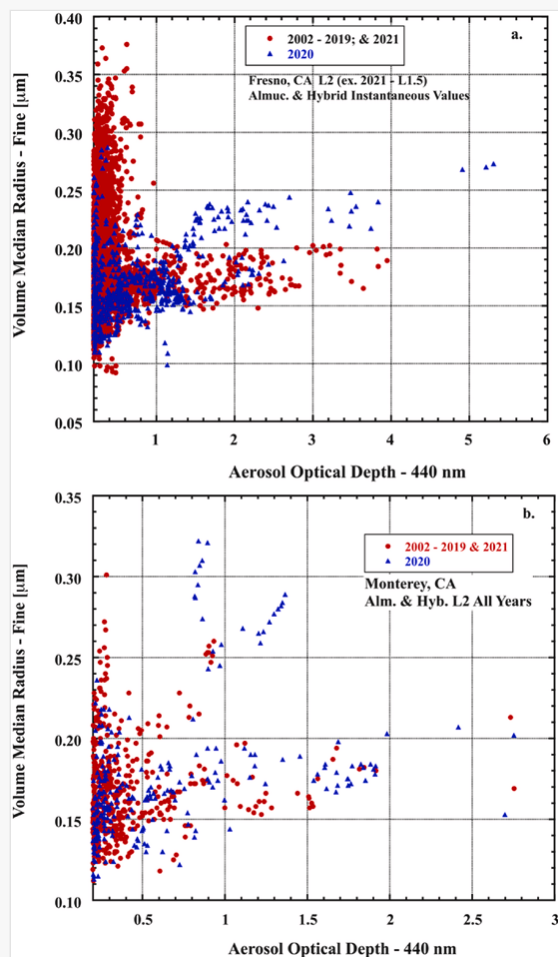
(a) Individual AERONET retrievals of fine mode volume median radius as a function of AOD (440 nm) for the Fresno site. Data from 2020 are plotted separately from all other years. Note that for all other years the majority of observations with AOD(440)>1 are mostly from 2021 with only 10 points from 2002 to 2019 combined. (b) Similar to (a) but for the Monterey AERONET site.

A similar examination of retrieved fine mode radius data for the Monterey site shows a more complicated relationship between fine mode volume median radius and AOD for the year 2020 as compared to what was observed at the Fresno site. In Fig. 4b at Monterey there is a very wide range in fine volume median radius ($\sim$0.15–0.32 μm) for the AOD range of 0.8–1.4 at 440 nm in 2020, therefore suggesting smoke from different fire sources, combustion conditions and aging processes exhibited a wide range in particle size at similar aerosol concentrations. This could potentially complicate some satellite retrievals of aerosol properties due to such large variation of particle size and associated scattering phase function. In 2021 there were no retrievals of fine mode radius that exceeded 0.22 μm, therefore

significantly smaller than the maximum radius observed in 2020, despite both years being extreme forest fire burning years in California.

3.2 Synoptic flow and aerosol transport during September 2020

In this paper we focus on September 2020 as an example of the dynamics and aerosol microphysics of continental scale plumes created by explosive western wildfire development and emissions. Daily area averaged MOD08/MYD08 MODIS AOD time series for western continental US (32-50º N; 109-125º W) with associated images from the Soumi NPOESS Partnership Project (SNPP) Visible and Infrared Imaging Radiometer Suite (VIIRS) along with day and night Terra and Aqua fire detections (orange) are provided in Fig. 5. Fire activity was already notable for the summer of 2020 with several significant fires present in mid July in northern California (e.g., Fig. 5a and (b)). After a brief respite, lightning activity from subtropical convection passing through the region on August 16, 2020 set off a series of fires from southern California through Washington, leading to significant fire activity and plumes that covered large areas of the western United States by August 19 (Fig. 5c). While fire weather and suppression improved after this initial regional fire development, several fires in Sierra Nevada, northern California and Oregon largely remained active for the next two weeks, but with more limited emissions. By September 6, 2020 meteorology again was more favorable to burning, and a renewed emissions event was initiated (Fig. 5d).

(i) Images are optimised for fast web viewing. Click on the image to view the original version.

alt-text: Fig. 5

Fig. 5
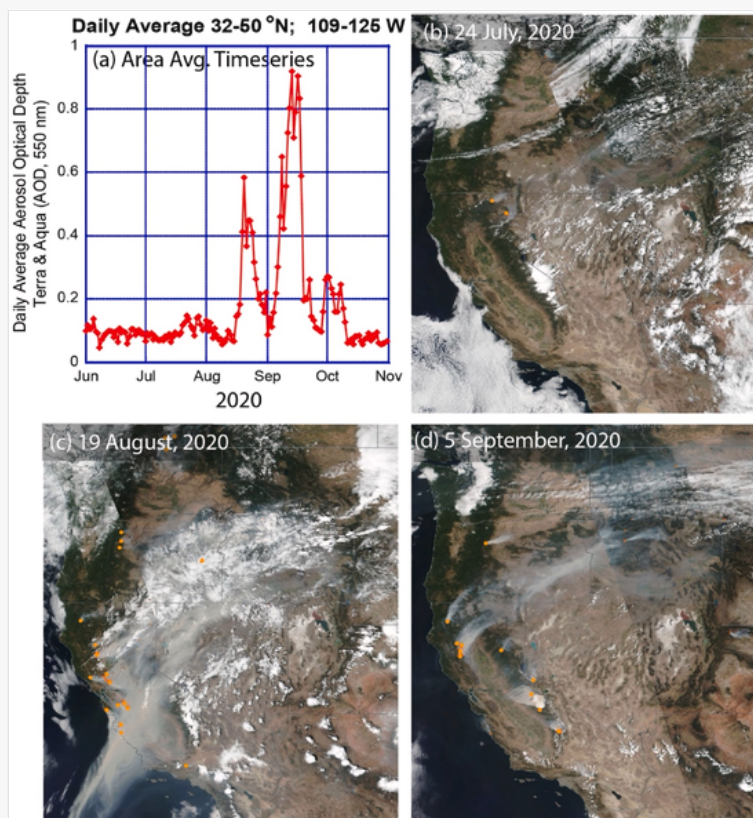
Aerosol optical depth time series and selected SNPP VIIRS true color images of the western CONUS 2020 fire season. (a) Daily average MOD08/MYD08 Dark Target/Deep Blue AOD for the domain of 32–50° N; 109–125° W. (b) VIIRS true color image of the domain in (a) for 24 July 2020 for one of the early seasonal peak smoke days. Marked in orange are larger fire complexes as detected by Terra and Aqua MODIS. (c) Same as (b) but for August 19, 2020 during a significant burning event blowup initiated by subtropical convection and lightning. (d) Nominally the same as (c) roughly two weeks later (on 5 September 2020) with reduced emissions.

For the transcontinental plumes analyzed in detail in this paper, a notable event developed after September 6 with strong winds and numerous new fires in Oregon, along with a switch in wind direction to regional offshore flow by September 8. By September 10, 2020, when fires were intense, plume injection was throughout the troposphere, and upper level offshore flow advected smoke over the Pacific Ocean. Fig. 6 provides an overview, with a) SNPP VIIRS

true color and Terra/Aqua fire detections, NAVGEM 400 hPa (∼7600 m) winds, and CALIOP nighttime (descending; 1035 UTC) orbit track; b) corresponding CALIPSO CALIOP nighttime 1064 nm attenuated backscatter; and c) CALIOP 1064 nm daytime attenuated backscatter collected 15 min after the VIIRS data collection. Here 1064 nm is used as optical extinction for smoke since at 1064 nm extinction is ∼40% less that at 532 nm, and hence there are smaller areas of total beam attenuation. Two basic plumes are visible. The dominant plume between 40° and 45° latitude was advected some 2000+ km offshore (as confirmed by the behavior of the wind vectors) and is between a midlevel anticyclone off of the Washington Coast and a low pressure system off of central California. A southern plume, covering southern California to Baja California, is seen wrapping around a low-pressure system that is over Utah and Colorado to the northeast, and an anticyclone offshore of Baja California. The VIIRS image is dramatic in its own right, but CALIOP data also demonstrates significant variability in the vertical. The southern plume is made of intricate levels from ∼5 km to the approximate level of the tropopause at 10 km altitude (∼550–280 hPa). The smoke is so thick that during daytime the plume fully attenuates the 1064 nm beam. For the northern plume, the CALIPSO orbit is not as ideal, but is the closest to the fires for this study period. Between 42° and 45° latitude, during the PM orbit smoke from a single fire is seen to be injected to 4−6 km. A second pass, at approximately 23:09 Z along the leading nose of the plume (40°-44° N; ∼146° W), showed an altitude range between 3 and 6 km. Thus, from a 2D perspective, VIIRS suggests one large plume, but in reality there were multiple plumes with generally higher plume altitudes to the south interacting with numerous mid-level weather systems.

alt-text: Fig. 6

Fig. 6
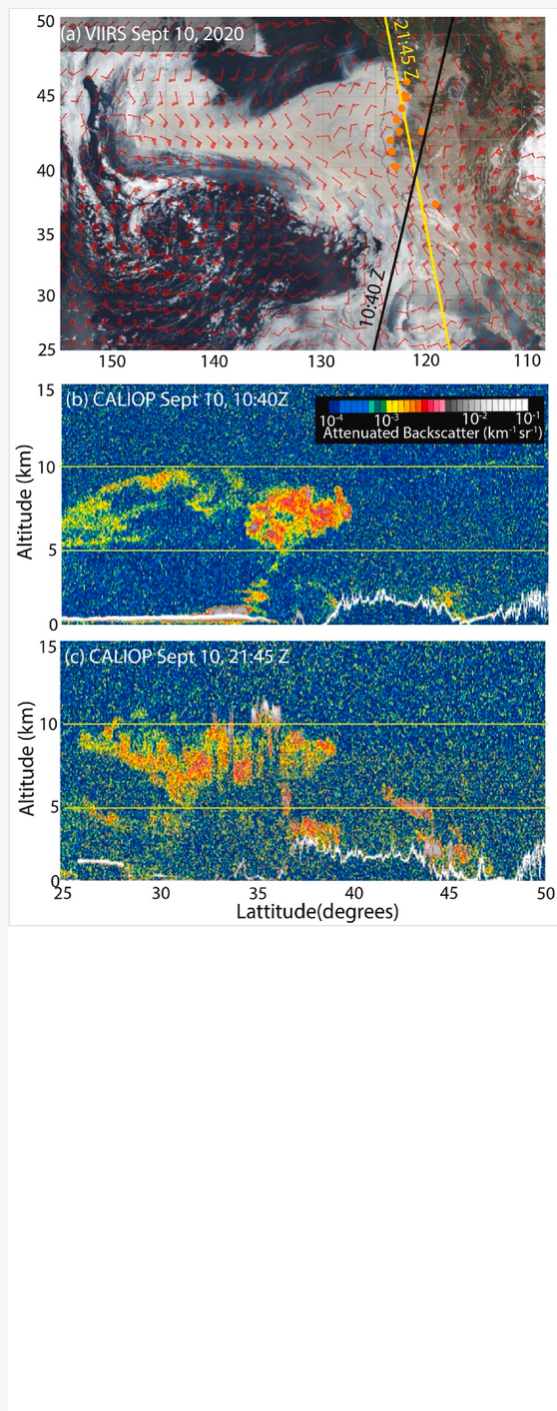
(a) SNPP VIIRS True Color Image for September 10, 2020 at 21:30 Z. (b) CALIOP 1064 nm 10:40Z (AM) attenuated backscatter profile, with track noted as black line on (a). (c) CALIOP 1064 nm 21:35Z (PM) attenuated backscatter profile, with track noted as yellow line on (a).

Over the subsequent days, the bifurcating northern and southern smoke plumes were transported across the United States and to the Atlantic Ocean, both serendipitously over the NASA Goddard Site in Maryland on September 14–15, 2020. This is demonstrated in a series of daily images in Fig. 7 from the SNPP VIIRS true color imagery with 400 hPa (~7600 m) NAVGEM winds on September 11 through 15, 2020. The 7.6 km wind field was chosen since several CALIPSO lidar aerosol vertical profiles across the continental US from September 12–15, 2020 measured the smoke layer located typically at ~6 km at the bottom to ~10 km at the top except for a descent in altitude near the east coast. On September 11 (Fig. 7) the overall west coast smoke plume has split into three components: 1) The northern high-pressure system moved onshore, bringing smoke back onto the Pacific Northwest; 2) the western most edge of the Pacific smoke plume is wrapping around the cyclone offshore of central California; and 3) the southernmost plume is advecting onshore towards the low that has advected eastwards from Utah and Colorado. By September 13 we can see the smoke well wrapped around the offshore cyclone; the northern anticyclone has morphed into a larger ridge advecting smoke into Canada and the upper Midwest; and the original Utah/Colorado low has migrated past the Great Lakes with a large cold front, bringing the southern smoke plume with it. By September 15 most of the United States is

covered with western biomass burning smoke, with the exception of areas influenced by hurricane Sally coming onshore in Alabama.
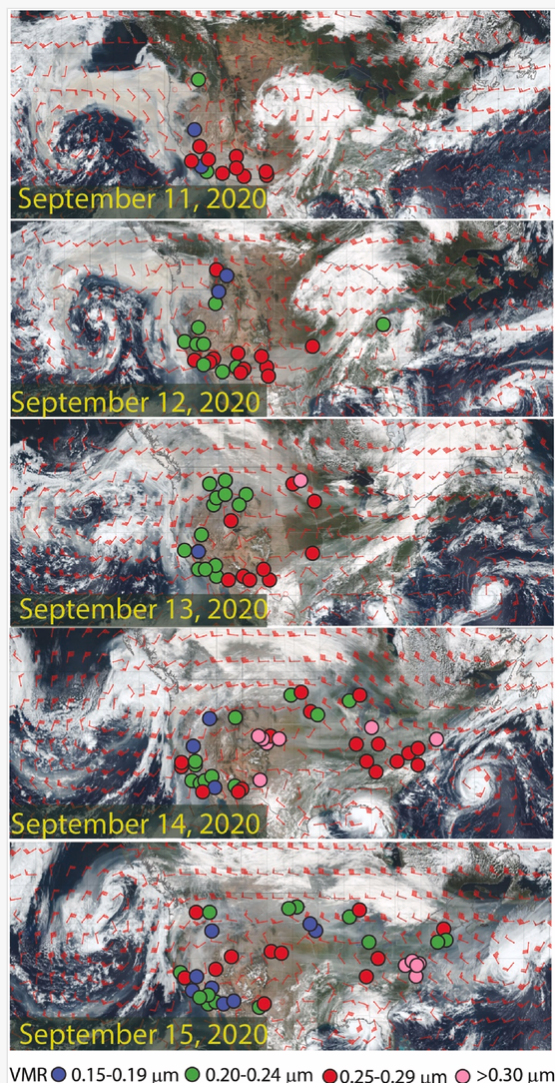
A time series of SNPP VIIRS true color images with NAVGEM 400 hPa winds corresponding to 11, 12, 13, 14 and 15 September 2020. Also shown are AERONET sites Level 2 retrievals of daily fine mode average volume median radius for each date.

Additionally in Fig. 7, the AERONET Level 2 daily average fine mode volume median radius values obtained from the almucantar and hybrid scan retrievals for all sites are shown superimposed. Starting on Sep 11, 2020 there was large variation in particle radius observed at sites in California, plus an eastward advection of large radius smoke (red markers) into Arizona and New Mexico originating from the elevated layer of smoke that was over the Pacific (see Fig. 6a). The advection of the large radius particles in the southern plume continues eastward on September 12 and 13 while on September 13 there are also large radius retrievals in the northern plume (also likely originated from the aged smoke layer over the Pacific) in North and South Dakota with fine radius at the NEON_WOOD site in North Dakota exceeding 0.30 μm (pink marker). On the next day, September 14, there is a wide range of particle radius in the west coast states while an aged plume has reached a cluster of four sites on Colorado (CO), with the retrieved radius at three of these sites exceeding 0.30 μm (two of these CO sites on this date are examined later in Fig. 10). Additionally on September 14 a large number of sites in the mid-West and mid-Atlantic region showed large particle radius retrievals exceeding 0.25 μm, with one site in Michigan and one on Long Island, New York exceeding 0.30 μm. On September 15 there continues to be a wide range in retrieved smoke particle radius in the western and north-central US states, while there was a cluster of five sites in Maryland and Virginia with very large radius smoke particles (>0.30 μm). A

nearly linear zonal plume of smoke from Colorado to the mid-Atlantic region is seen in these VIIRS images, suggesting the possibility of this extremely large particle smoke being transported almost directly eastward from September 14 to 15. Overall this series of images shows a wide variation in particle radius across the US during the peak of this extreme event, likely due to variation in both fire characteristics and particle aging, and also suggestion of particle size growth due to coincident aging and transport processes.

Both the northern and southern smoke plumes were observed by the combined GSFC AERONET sun-sky radiometer and MPLNET lidar over the September 14–16 time period (Fig. 8 (a)). The NASA Micro Pulse Lidar Network (MPLNET) is a global network of Micro Pulse Lidar instruments co-located with AERONET (Welton et al., 2001). The MPLNET normalized relative backscatter (NRB) signals at 532 nm are described by Campbell et al. (2002). The first smoke arrival was on September 14 at 12:00 Z at ~5 km. By 21:00 Z, parts of this plume was observed at altitudes of nearly 10 km. Aerosol optical depths measured by AERONET were ~1 in the mid visible (500 nm). Taking the center of this plume feature to be at 8 km at 18Z, a 120 h HYSPLIT back trajectory (Stein et al., 2015) was performed with 1/4° GFS data (Fig. 8 (c)). The trajectory shows this to be associated with the southern plume, where smoke was transported from the southwest and Midwest behind a cold front. A second more optically thick (AOD reaching 1.5) and prolonged smoke plume arrived on September 14 21Z at an altitude of ~5 km. This plume just arrived as the upper plume left the region with some overlap, and remained until September 17 with progressively lower altitudes, bottoming out at ~3 km. A trajectory computed for the densest part of the plume on September 15, 12Z shows this plume to be associated with the northern transport pathway. Thus, western US fire plumes taking quite different transport routes were influencing the same site on the east coast of the United States.

(i) Images are optimised for fast web viewing. Click on the image to view the original version.

alt-text: Fig. 8

Fig. 8
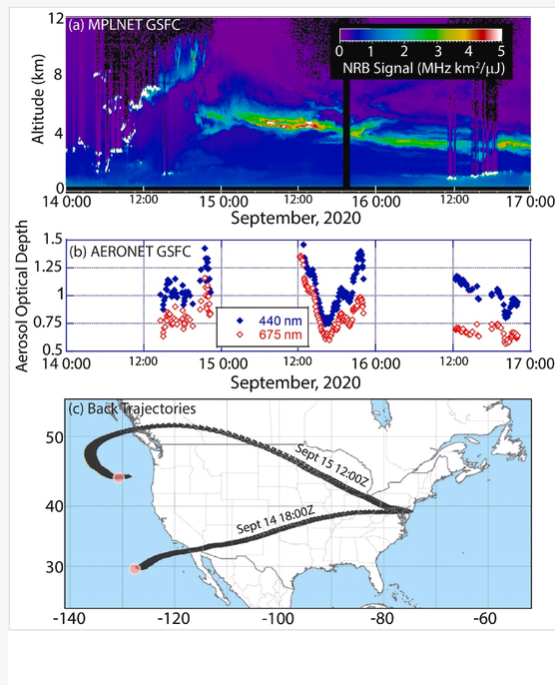
MPLNET lidar profiles and HYSPLIT back trajectories for the NASA GSFC site in Greenbelt MD. a) MPLNET normalized relative backscatter (NRB) image from September 14 through 16. b) Mid visible aerosol optical depth measured at the GSFC AERONET site corresponding to the MPLNET lidar observations. c) NOAA HYSPLIT 120 h back trajectories computed from Sept 14 18Z for 8 km and September 15 12:00 Z at 5 km.

3.3 Aerosol properties in September 2020 at California AERONET sites and comparison to a long-range transport case in Maryland

The measured AOD spectra of several cases of biomass burning smoke in September 2020 at different sites and dates in California plus the long-distance transported smoke to GSFC from the west coast on Sep 15, 2020 are shown in Fig. 9a. Throughout this study we normalize each AOD spectra to its value at 500 nm in order to facilitate comparisons between sites. First, note that the AOD spectra for the 2020 smoke transport case at GSFC is very unusual, given the maximum AOD at 500 nm and significant decrease in AOD at wavelengths shorter than 500 nm. This anomalous AOD spectra is extremely rare within the 29-year monitoring history of the AERONET network. Most AOD spectra from California sites which were nearer to the fire locations showed more typical spectra where AOD continued to increase as wavelength decreased. However the Table Mountain, CA (east of Los Angeles) case on Sep 12 showed a similar AOD spectra to GSFC despite being much closer to the fire sources. Note that this plot is in logarithmic coordinates in both axes and that none of these cases exhibited linear or even near-linear AOD spectra which would occur for AOD spectra governed by a more traditional Angstrom fit. In Fig. 9b of the retrieved volume size distributions for these same cases, some cases in California show smaller radius and wider fine mode distributions than was retrieved for this GSFC case. We have normalized the volume size distributions of all sites to the peak value of the distribution for each individual site, again to make clearer comparisons between sites. Note that the curve fits in this figure are cubic splines to the retrieved size distribution values at 22 distinct radii values, therefore the curve fits sometimes overshoot the normalized maximum 1.0 value in the plots. Consistent with its similar AOD spectra, the Table Mountain, CA case on Sep 12 is approaching the large fine mode particle size and narrow width of the GSFC case. This suggests that the smoke may have aged and coagulated/condensed over the Pacific before being transported eastward. Note that smoke from individual fires mixed with smoke from numerous other fires plumes that were burning over a period of days and remained in an elevated layer over the ocean (see Fig. 6 for Sep 10 and Fig. 7 for Sep 11) for a few days before reversing direction and then advecting eastward to the sites. Therefore smoke from individual fires were not likely to maintain their unique properties after mixing with smoke from other fires plus undergoing aging and reactions with particles and gases from other plumes. The spectral single scattering albedo for these cases are shown in Fig. 9c. Note the significant decrease in SSA from 675 to 440 nm suggesting significant BrC and/or coated BC absorption at some of these sites. The SSA spectra at Table Mountain, CA on Sep 12 and Fresno on Sep 11 shows similar or greater decrease from 675 nm to 440 nm to the one retrieved at GSFC on Sep 15, suggesting that there was similar or greater spectral absorption signature in that particular smoke that was still in CA but that was very likely aged first in an elevated layer over the Pacific. Also note that the strong spectral SSA signature at the GSFC site suggests the possibility that BrC has a significant lifetime of greater than ~4–5 days (if the absorption had a significant BrC component), longer than sometimes suggested in the literature (Wong et al. (2019)). However Di Lorenzo et al. (2017, 2018) found that the majority of BrC absorption occurred in the larger mass (sized) biomass burning particles and that these particles continued to absorb after aging. This is consistent with the absorption measured in the large size aerosol that were observed at the Fresno, Table Mountain and GSFC sites. Additionally Wong et al. (2017) observed that the larger molecular weight biomass burning particles remained the most absorbing of the BrC compounds with aging. Laboratory smoke experiments of Fleming et al. (2020) found that degradation of BrC due to UV irradiation was slowest for coniferous tree fuels (lasting ~ 1 month) and also appeared to be dependent on the combustion conditions with flaming phase resulting in longer lifetime. This very long lifetime of BrC in the lab for coniferous fuels under UV exposure suggests that oxidation by hydroxyl radicals in the atmosphere may be a major factor in BrC degradation. The extreme forest fires in Sep 2020 in CA/OR were dominated by coniferous tree fuels with intense crown fires burning with significant flaming phase combustion followed by continuing smoldering combustion of woody fuels. However we emphasize that it is entirely possible that coated BC either exclusively or in combination with BrC may be the reason for the lower SSA at 440 nm relative to 675 nm. Another aspect to consider in the short wavelength absorption by BrC and/or coated BC is that it is possible that some of the absorption occurs in gases rather than particles. Chen et al. (2021) present measurements that show that up to 40% of the absorption due to BrC at 400 nm was due to the gas phase BrC. Therefore it is possible that the AERONET measurements of absorption at short visible to UV wavelengths are a result of both the combined gas and particle phase BrC that attenuate the measured sky radiances. However this BrC gas absorption was measured by Chen et al. (2021) for pollution cases in a large city in China, and not for biomass burning smoke gases therefore it is unknown if such gaseous absorption occurs for forest fire smoke. Additionally, nitrogen dioxide (NO_2) is produced during biomass burning (Griffin et al., 2021) and therefore some of the absorption attributed to aerosols in the AERONET retrievals may be due to NO_2 absorption especially at 380 and 440 nm. NO_2 lifetime is relatively short however (typically hours) so this is mainly a factor relatively near to the fire source and thus not a likely significant factor in the cases presented here.

alt-text: Fig. 9

Fig. 9
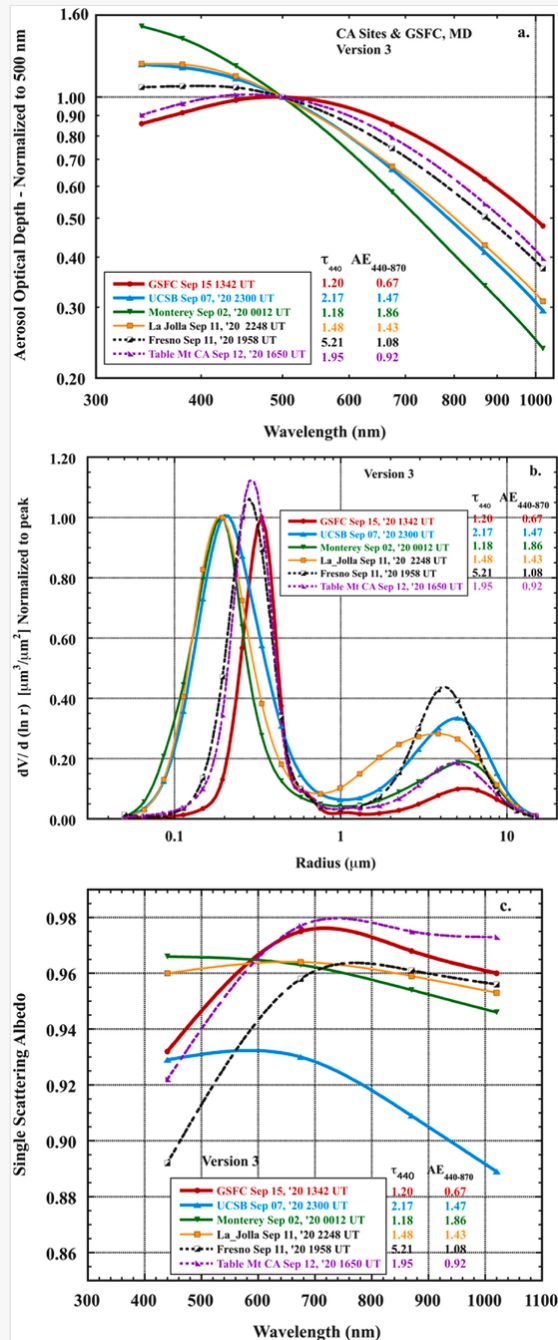
(a) The measured AOD spectra of several cases of biomass burning smoke in September 2020 at different sites and dates in California plus the long-distance transported smoke at GSFC on Sep 15, 2020. Each AOD spectra is normalized to its value at 500 nm in order to facilitate comparisons between sites. (b) The retrieved volume size distributions for these same cases; some cases in California show smaller radius and wider fine mode distributions than was retrieved for the GSFC case. The volume size distributions of all sites have been normalized to the peak value of the distribution for each individual site, again to make clearer comparisons between sites. (c) The spectral single scattering albedo for these same cases.

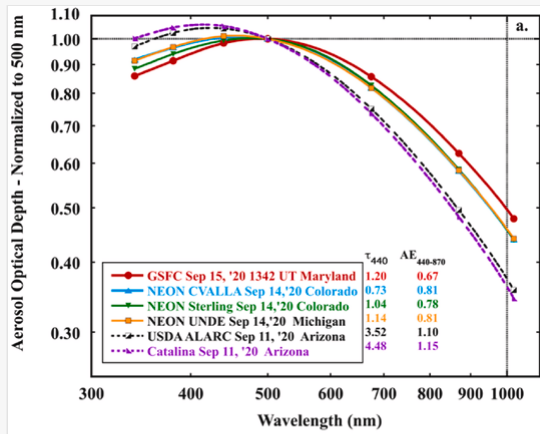## 3.4 Examination of measurements of anomalous AOD spectra with maxima at or near 500 nm

Several other AERONET sites measured anomalous AOD spectra in Sep 2020 similar to or approaching the one observed at GSFC on Sep 15, 2020, with decreasing AOD as wavelength decreased below 500 nm or 440 nm. These

cases all occurred between Sep 11 and 14 at sites in Arizona, Colorado, and Michigan (Fig. 10a) from smoke plumes advected from the major fire sources in California and Oregon (after aging over the Pacific Ocean). The AOD spectra in Colorado and Michigan are close to the GSFC spectra, just slightly less extreme. All of these selected long-distance transported CA/OR smoke cases (Fig. 10b) have large radius and relatively narrow volume size distributions from the AERONET retrievals. The size distributions in NEON_CVALLA (Colorado) and NEON_UNDE (Michigan) are also nearly as narrow as was retrieved at GSFC. Therefore all of these aerosol cases are likely of relatively aged particles, coagulated plus enhanced condensation smoke that have resulted in these very large size fine mode particles. The absorption (SSA) spectra associated with these cases are compared in Fig. 10c. For all of these cases of aged and transported CA/OR forest fire smoke the SSA at 440 nm is significantly less than at 675 nm (by $\sim$0.03$-\sim$0.05), therefore strongly suggesting significant BrC and/or coated BC absorption.

Images are optimised for fast web viewing. Click on the image to view the original version.

alt-text: Fig. 10

Fig. 10

a.

	τ_{440}	$AE_{440-870}$
GSFC Sep 15, '20 1342 UT Maryland	1.20	0.67
NEON CVALLA Sep 14,'20 Colorado	0.73	0.81
NEON Sterling Sep 14,'20 Colorado	1.04	0.78
NEON UNDE Sep 14,'20 Michigan	1.14	0.81
USDA ALARC Sep 11, '20 Arizona	3.52	1.10
Catalina Sep 11, '20 Arizona	4.48	1.15

b.

c.

Version 3

	τ_{440}	$AE_{440-870}$
GSFC SEP 15, '20 1342 UT Maryland	1.20	0.67
NEON CVALLA Sep 14,'20 Colorado	0.73	0.81
NEON Sterling Sep 14,'20 Colorado	1.04	0.78
NEON UNDE Sep 14,'20 Michigan	1.14	0.81
USDA ALARC Sep 11, '20 Arizona	3.52	1.10
Catalina Sep 11, '20 Arizona	4.48	1.15

(a) Normalized AOD spectra (to 500 nm for each retrieval) for selected cases between Sep 11 and 14, 2020 at sites in Arizona, Colorado, and Michigan from smoke plumes advected from the major fire sources in California and Oregon. These AERONET sites/cases were selected since they exhibited anomalous AOD spectra similar to or approaching the one observed at GSFC on Sep 15, 2020, with decreasing AOD as wavelength decreased below 500 nm or 440 nm. (b) Normalized volume size distributions (to maximum concentration for each retrieval) of these same selected long-distance transported smoke cases show large radius and relatively narrow volume size distributions from the AERONET retrievals. (c) The retrieved spectral SSA of these same cases are compared. For all of these sites/cases of aged and transported smoke the SSA at 440 nm is significantly less than at 675 nm thereby strongly suggesting significant BrC and/or coated BC absorption.

Since the unusual AOD spectra at GSFC on the morning of Sep 15, 2020 was nearly unprecedented in the ~29 years of AERONET monitoring we examine it in more detail here in order to explain and understand this phenomenon. Fig. 11a shows extreme differences in Angstrom Exponent as a function of wavelength at this site and date that occurred due to the large radius (Eck et al., 1999) and narrow size distribution width of the fine mode dominated smoke particles. We provide Angstrom exponents in different spectral intervals since atmospheric aerosol studies extensively utilize the AE as a parameter to characterize the basic size of atmospheric particles. However, a second order fit to the AOD spectra is much better, as shown in Fig. 12a. These AE values in Fig. 11a are all computed from multiple wavelengths (3 or 4) by linear regression of AOD versus wavelength in logarithmic coordinates. The AE(380–500 nm) was negative at −0.32 in the early morning while at the longest wavelengths (870–1640) it was 2.29. The time of the GSFC case that is shown in the other figures was at 1342 UTC in the morning therefore at the minimum value of AE(380–500). The coarse mode AOD was ~0.01 (from both Dubovik and SDA retrievals) out of a total extinction AOD(440) of 1.20 at 1342 UTC (AOD daily range of 1.55 to 0.8 at 440 nm), therefore the mid-visible fine mode fraction (FMF) was >0.99 at that time. The short wavelength AE(380–500 nm) is most sensitive to fine mode particle size (Reid et al., 1999; Eck et al., 2014) showing an increasing trend throughout most of the day while the long wavelength AE (870–1640 nm; more dependent on fine mode fraction) was relatively constant throughout the day. The fine mode volume median radius retrieved by the Dubovik algorithm from almucantar and hybrid scans decreased from a maximum of ~0.32 μm in the early morning to a minimum (but still large size) of ~0.27 μm in the late afternoon (Fig. 11b). The fine mode width (std. dev.) was also significantly narrower in the morning at 0.33 (geometric std dev = 1.39) increasing to a maximum of ~0.41 in the afternoon (geometric std dev = 1.51). Therefore the smoke plume on Sep 15 at GSFC showed significant variation in aerosol size distribution throughout the daytime hours of this day suggesting variable conditions in both the source fires and in the particle aging and transport processes.

alt-text: Fig. 11

Fig. 11
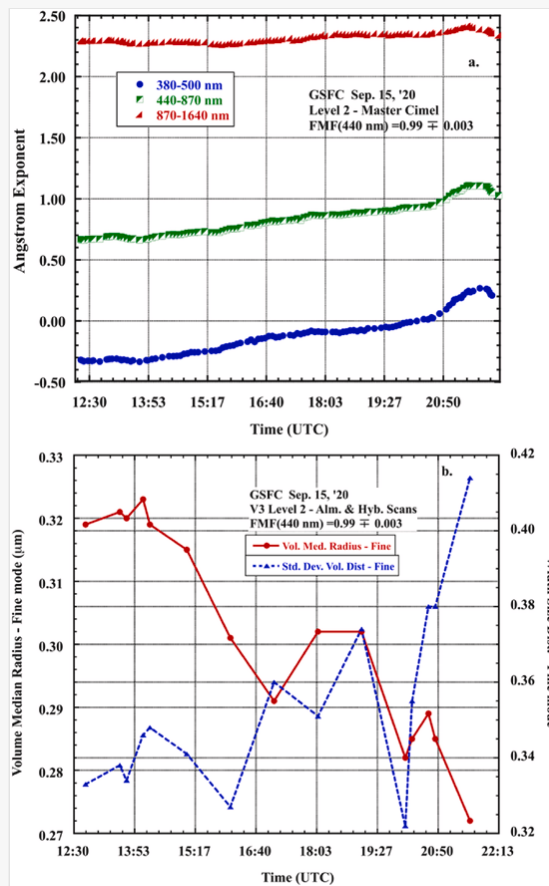
(a) Time series of Angstrom Exponent as a function of wavelength at GSFC on Sep 15, 2020, with very large spectral variation due to the large radius and narrow size distribution width of the fine mode dominated smoke particles. These AE values are all computed from multiple wavelengths (3 or 4) by linear regression of AOD versus wavelength in logarithmic coordinates. The AE(380–500 nm) was negative at −0.32 in the early morning while at the longest wavelengths (870–1640 nm) it was 2.29. (b) Time series of the fine mode volume median radius and width retrieved by the Dubovik algorithm from almucantar and hybrid scans for the same site and date as in (a).

alt-text: Fig. 12

Fig. 12
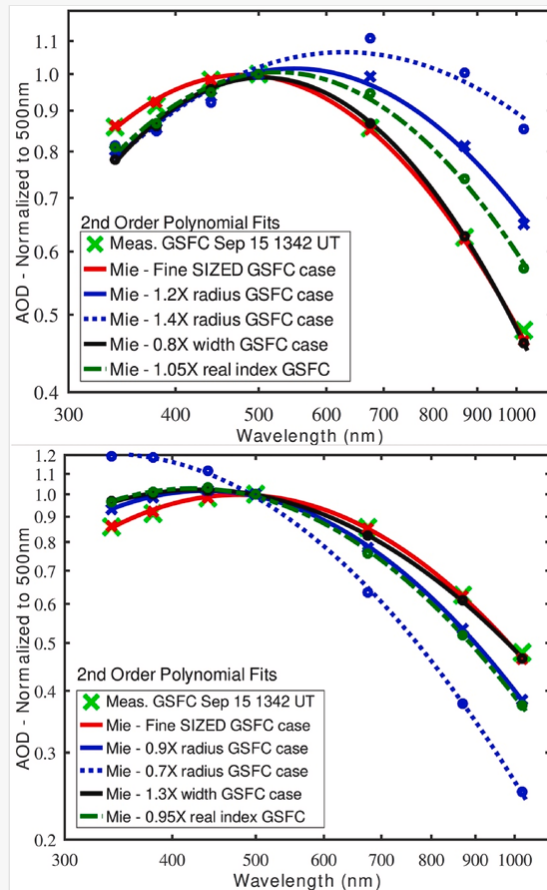
(a) Mie calculations of AOD spectra (normalized to 500 nm) in order to explore the effects of fine mode particle radius, fine mode width and index of refraction. Additionally the AOD spectra measured at the Goddard site on the morning of Sep 15, 2020 are shown in large light-green crosses. The curves in this figure are 2nd order polynomial fits of AOD versus wavelength in logarithmic coordinates. All of these simulated cases resulted in even greater reductions in AOD for wavelengths less than 500 nm. (b) Mie simulations with perturbations to the same parameters as in (a) relative to the case observed at GSFC on Sep 15, 2020, however all of these modifications (smaller radius, larger width, smaller real part) resulted in smaller decreases (or even increases) in AOD for wavelengths shorter than 500 nm and in lower AOD for wavelengths longer than 500 nm.

The GSFC site was not the only one on the east coast on Sep 15, 2020 to measure very anomalous AOD spectra associated with this aged smoke plume. Nearby sites in Maryland, one in Baltimore (MD_Science_Center) and another south of Annapolis (SERC), sites located <37 km from GSFC, both showed similar early morning Level 2 measurements of AOD spectra with maxima at 500 nm (exceeding the 440 nm AOD by ~0.02) and similar retrieved size distributions. The site of NASA_LaRC (NASA Langley Research Center) in coastal Virginia and the CCNY (City College of New York) site in New York City also showed similar spectra although less extreme than measured at GSFC. The CCNY site is 319 km north-east of GSFC and the NASA_LaRC site is 214 km south of GSFC. However both sites showed AOD at 440 nm greater than at 500 nm, while at GSFC in the early morning it was 0.02 less than at 500 nm. Also the retrieved size distributions at these sites showed somewhat smaller radius and wider fine mode than at GSFC. The retrieval of volume median radius at the NASA_LaRC site (Level 2) was 0.31 μm and at CCNY was 0.28 μm (Level 1.5) while at GSFC it was somewhat larger at 0.32 μm. The retrieved fine mode width was also narrower at GSFC (0.33; geom. std. dev = 1.39) versus 0.39 (geom. std. dev. = 1.48) at NASA_LaRC and 0.38 (geom. std dev. = 1.46) at CCNY.

To further analyze the reasons for the anomalous AOD spectra observed at GSFC on the morning of Sep 15, 2020 we performed a series of Mie calculations to explore the effects of fine mode particle radius, fine mode width and index of refraction on the AOD spectra. In Fig. 12a the AOD spectra normalized to 500 nm measured at the Goddard site on the

morning of Sep 15, 2020 are shown in large light-green crosses. Mie calculations using the retrieved fine mode size distribution and refractive index on this same site/time are shown in solid red and match the measurements within 0.01. The lines in this figure are 2nd order polynomial fits of AOD versus wavelength in logarithmic coordinates (Eck et al., 1999), which fit the measurements of the GSFC case to within ~0.01 at all wavelengths. Additionally, Mie computed AOD spectra are shown with size distributions modified relative to the retrieved distribution: 2 cases of increased radius while the width is held constant and one case of decreased width with same radius as the measured size distribution. One case of a 5% increase in real refractive index relative to the retrieved values is also shown. The retrieved real refractive index ranged from 1.56 at 440 nm to 1.52 at 1020 nm. All of these modifications resulted in larger decreases in AOD for wavelength shorter than 500 nm and in higher AOD for wavelengths longer than 500 nm. Changes in AOD spectra due to a 20% increase in the imaginary part of the refractive index were also computed, however the effect was insignificant. Note that the most extreme case of 1.4X the radius of the GSFC case (shown in blue circles in Fig. 12a) yields a volume median radius of ~0.48 μm and peak AOD at 675 nm. This type of size distribution would cause a blue colored sun due to greater extinction in the red wavelengths, as was famously observed in Scotland in 1950 in smoke transported from fires in western Canada (Wilson, 1951). Blue and green colored suns were also observed due to aged stratospheric aerosol from some major volcanic eruptions, most notably from Krakatoa in 1883 (Larrabee, 1884). Research by Wilson (1951) and Ehlers et al. (2014) found that aerosol size distributions with dominant radius from 0.4 to 0.7 μm result in a spectral increase in aerosol scattering coefficients at longer wavelengths in the visible and therefore could result in blue colored suns if coupled with a narrow sub-micron size distribution. Wullenweber et al. (2021) recently investigated the physical reasons for the historical occurrences of these blue colored suns. They argued using simulations that anomalous extinction by atmospheric particles of specific sizes and narrow size distribution can explain the phenomenon of blue suns. They also found both water vapor absorption and ozone absorption to be minor factors in causing blue colored suns. Although the blue sun phenomenon was not observed in the smoke case presented here, the observed AOD spectra and retrieved size distribution for this September 15, 2020 GSFC case were the closest ever measured (in 30 years of AERONET monitoring) to approaching the extremes required for this phenomenon to occur.

In order to investigate the opposite effects on spectral AOD that would be caused by decreases in particle radius, increases in width of the fine mode size distribution and decrease in real refractive index, we performed additional Mie simulations with perturbations to the case observed at GSFC on Sep 15, 2020 (Fig. 12b). All of these modifications resulted in smaller decreases (or even increases) in AOD for wavelengths shorter than 500 nm and in lower AOD for wavelengths longer than 500 nm. This further confirms that only large radius and narrow widths of sub-micron aerosol size distributions can cause greater extinction in longer mid-visible wavelengths relative to the shorter-wavelength visible and UV.

A search of the entire AERONET Version 3 Level 2 data base was performed to find fine mode dominated cases of extremely anomalous AOD spectra (similar to the GSFC Sep 15, 2020 case) where the maximum AOD occurred at 500 nm. The criteria for the search was AOD at 500 nm exceeding the 440 nm AOD by 0.02 or more (same as the GSFC case), 440 nm exceeding 380 nm by 0.02 or more and 380 nm exceeding 340 nm AOD by 0.02 or more. Three cases were identified: two from smoke aerosol originating from forest fires in Canada and one was at Arica, Chile of cloud processed sulfate aerosol. The first smoke case was at the Churchill site in Manitoba on the western shore of Hudson Bay on May 20, 2019. There is only one instantaneous measured AOD spectra that met these criteria and passed the cloud screening and quality control checks. The AOD was very high at 3.37 at 500 nm, 3.32 at 440 nm, 3.08 at 380 nm and 2.85 at 340 nm. Therefore this case was one that greatly exceeded the 0.02 AOD thresholds for decreasing values at shorter wavelengths. The AE(440–870 nm) was 0.68, and AE(380–500) was −0.30 both nearly identical to the anomalous case at GSFC (see morning in Fig. 11a). Large forest-fire hot spots with associated heavy smoke plumes were noted in MODIS imagery over the Canadian province of Alberta on May 18–20, 2019: these hot spots were likely the source of this aerosol event. This implies that the particles achieved the large sub-micron sizes necessary to produce this anomalous spectra with only 1–2 days of plume aging. The second smoke case of anomalous AOD spectra was at the NEON_UNDE site in northern upper peninsula Michigan (USA) on August 17, 2018. The smoke source in this case was a cluster of several fires in British Columbia which started producing large and heavy smoke plumes on August 09 although the fires began before that. Back trajectories computed from HYSPLIT suggest that the smoke transit time from the fires to the NEON_UNDE site was ~2–3 days, although this is somewhat uncertain since the height of the plume is unknown. Again, there is only one instantaneous measured AOD spectra that met these anomalous spectra criteria. The AOD was very high 5.36 at 500 nm, 5.34 at 440 nm, 5.05 at 380 nm and

4.71 at 340 nm. Therefore this case just barely exceeded the 0.02 AOD difference threshold from 500 nm versus 440 nm. However several other AOD spectra on this site/date are very similar but the AOD at 440 nm is either nearly equal or slightly greater than the 500 nm AOD. The AE(440–870 nm) was 0.77, and AE(380–500) was −0.22 therefore similar but slightly less extreme compared to the anomalous case at GSFC (see Fig. 11a). There were no AERONET sky radiance scan retrievals coincident with the anomalous AOD spectra in the thick part of the plumes on both of these days, and as a result no ability to investigate the retrieved size distributions associated with these cases. There was extensive snow and ice at Churchill on May 20, 2019 so that would have precluded a high quality retrieval anyway due to the associated large uncertainty in surface reflectance (an input to the retrieval). These two cases of extreme AOD spectra with maxima at 500 nm occurred in 2018 and 2019 while the case measured at GSFC occurred in September 2020. This suggests a possible recent increase in probability towards severe and unusual burning conditions that resulted in very large fine mode particles with narrow size distribution width.

The other case with anomalous measured AOD decreases at all wavelengths less than 500 nm occurred at Arica, Chile on Sep 01, 2001. While this case is not a biomass burning aerosol case it is the only fine mode-dominated one in the entire 30-year AERONET database with anomalous AOD spectra (440 nm < 500 nm) that also had a Level 2 almucantar retrieval of size distribution and absorption parameters. This spectral AOD case and another from Arica are compared to the GSFC anomalous case from the morning of Sep 15, 2020 in Fig. 13a. The fine mode fraction of AOD at 440 nm was >0.95 for both of the Arica cases and >0.99 for the GSFC case. Note that the magnitude of the AOD decrease for $\lambda < 440$ nm is much smaller for the Arica case of Sep 01, 2001 compared to the GSFC case. In Fig. 13b of the retrieved size distributions the fine mode radius is even larger for the Arica, Chile cases than for the GSFC smoke case, however the width of the fine mode size distribution is much narrower in the GSFC smoke case. These retrievals of large fine mode particles in Arica (within 2 km of the Pacific Ocean coast) are a result of fog and/or stratocumulus cloud processing (Eck et al., 2012) of SO_2 emissions from copper smelter emissions. Version 3 retrievals of SSA for these same 3 cases are shown in Fig. 13c. The SSA for the Arica cases are very high, almost non-absorbing, consistent with the dominant sulfate aerosol type as contrasted with the strong absorption at 440 nm for the GSFC smoke case, indicative of BrC and/or coated BC absorption. Note that the Angstrom Exponent (440–870 nm) for all of these cases was very low for fine mode dominated aerosol, ranging from 0.67 for this GSFC case to 0.45 (Sep 1) and 0.78 (Jul 13) for the two cases at Arica, Chile. This results in a relaxed constraint for the spectral variation of the imaginary refractive index in V3. Utilization of relaxed constraints for fine mode cases at much higher AE is being investigated by the AERONET team for use in a future Version 4 database. More discussion of this issue is presented in section 3.6 below and in Sinyuk et al. (2022).

(i) Images are optimised for fast web viewing. Click on the image to view the original version.

alt-text: Fig. 13

Fig. 13
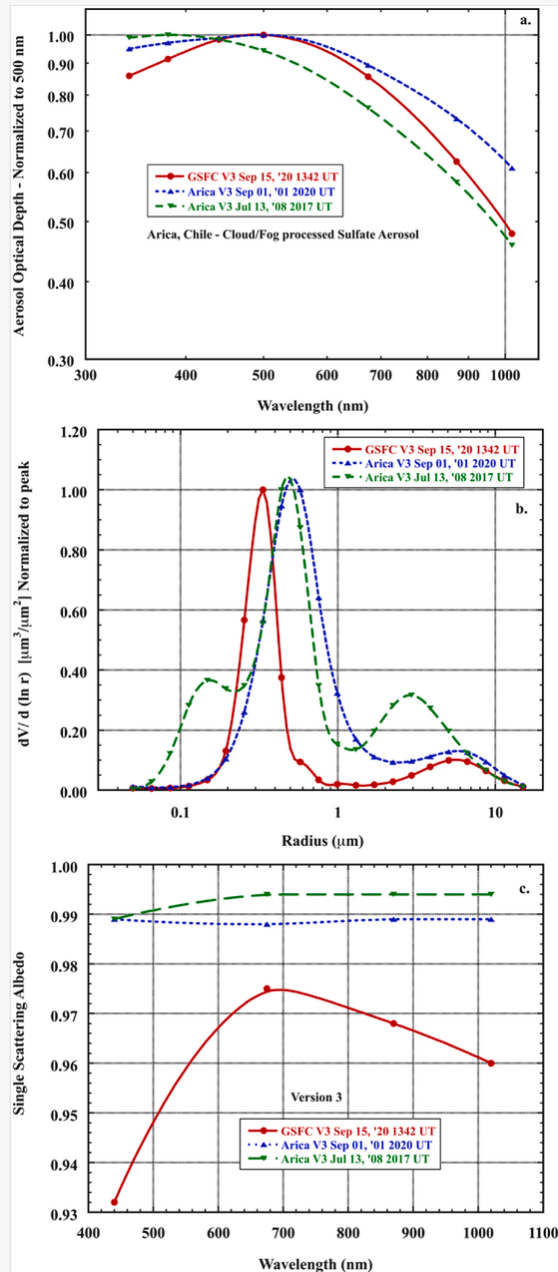
(a) Normalized AOD spectra for two cases at the Arica, Chile site are compared to the GSFC case from the morning of Sep 15, 2020. The fine mode fraction of AOD at 440 nm exceeded 0.95 for both of the Arica cases and >0.99 for the GSFC case. (b) Normalized retrieved size distributions showing even larger fine mode radius for the Arica, Chile fine mode cases than for the GSFC smoke case, however the width of the fine mode size distribution is much narrower in the GSFC smoke case. (c.) The spectral SSA for the Arica cases are very high, almost non-absorbing, as contrasted with the strong absorption at 440 nm for the GSFC smoke case.

## 3.5 Comparison of smoke aerosol properties in Sep 2020: long-range transport sites in the US

In this section we compare the aerosol properties measured and retrieved at selected AERONET sites at various distances from the main forest fire sources in CA and OR. Sites and cases were selected to have high AOD so that the accuracy of the retrievals of SSA have small uncertainties (Sinyuk et al., 2020). The AOD at 440 nm for these six cases ranged from 0.93 to 4.21 and the fine mode fraction of AOD at 440 nm exceeded 0.97 for all cases. These cases were chosen from a relatively short time interval from September 13 to 17, 2020 to obtain an idea of the amount of variability in the smoke aerosol optical and physical properties during the peak of the smoke transport eastward across North America. In Fig. 14a we compare the AOD spectra associated with these six AERONET sites in various US states and at different distances from the fire sources. The GSFC site (Maryland) case on Sep 15 is included here and the other sites are PNNL (Washington state), Missoula (Montana), NEON CVALLA (Colorado), Sioux Falls (South Dakota), and NEON UNDE (Michigan). The AOD spectra of these selected cases of transported biomass burning smoke from the CA/OR source region show varying amounts of spectral curvature but none show a decrease in AOD as AOD decreases for wavelengths <500 nm, as was observed at the GSFC site. The AE(440–870 nm) ranged from 0.67 at GSFC to 1.70 at Sioux Falls which is an extremely wide range of AE values for fine mode smoke. The AE(380–500 nm) ranged from −0.33 at GSFC to 1.05 at Sioux Falls, indicative of large variation in fine mode size distributions

(Eck et al., 2014). The retrieved size distributions of transported biomass burning smoke for these same cases from Sep 13–17, 2020 show significantly smaller radius and wider size distribution widths than the Sep 15 observations at GSFC (Fig. 14b). The volume median radius of these cases ranged from 0.18 μm to 0.29 μm as compared to 0.32 μm at GSFC, a very wide range of particle sizes from the extensive west coast biomass burning source region, again implying a range of combustion conditions, fuels and aging processes. This is consistent with the wide range in fine mode particle radius retrieved at the Monterey site (Fig. 4b) relatively near to some of the large fires locations in CA, and also consistent with the large variability in particle radius in various US locations shown in Fig. 7. The width of the fine mode (Fig. 14b) also exhibited a wide range from a standard deviation of 0.41–0.50 (geom. std dev. = 1.51 to 1.65) compared to 0.33 (geom. std dev. = 1.39) at GSFC. At most of these sites the AERONET retrievals of single scattering albedo (V3 here) show SSA lower at 440 nm than at 675 nm suggesting significant BrC and/or coated BC absorption (Fig. 14c). The exception is Sioux Falls, which also showed the steepest AOD spectra (highest AE) and the smallest particle size. However since these are V3 retrievals the higher AE at the Sioux Falls site imposes a stronger algorithmic constraint on the spectral variation of imaginary refractive index thereby forcing a relatively spectrally constant imaginary refractive index more typical of some BC cases (see discussion in section 3.6 below). The range in SSA across these sites at both the 675 nm and 440 nm wavelengths was ~0.02. The retrieved large spatial and temporal variability of smoke particle size and spectral absorption from this major biomass burning event poses a significant challenge to satellite remote sensing since certain aspects of both particle size distribution and absorption are often assumed a priori in some retrieval algorithms. For example the satellite retrieval algorithms of Remer et al. (2005) and Lyapustin et al. (2018) require a priori specification of aerosol absorption and utilize AERONET retrievals of imaginary refractive index and/or single scattering albedo as the source of these regionally varying values.

ⓘ Images are optimised for fast web viewing. Click on the image to view the original version.

alt-text: Fig. 14

Fig. 14
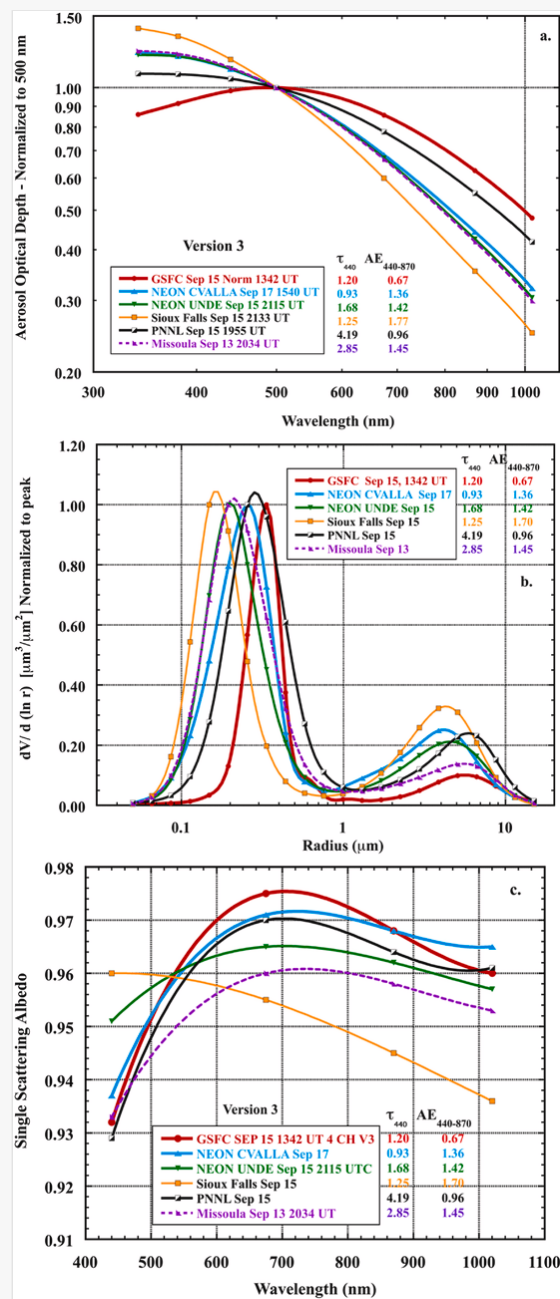
(a) Normalized AOD spectra associated with six AERONET sites in various US states and at different distances from the fire sources. These cases were chosen from the relatively short time interval of September 13–17, 2020 to examine the variability in the smoke aerosol optical and physical properties during the peak of the smoke transport eastward across North America. (b) Normalized size distribution retrievals of transported biomass burning smoke for these same cases. (c) Spectral SSA retrieved for these same sites, showing SSA lower at 440 nm than at 675 nm at most sites.

3.6 Smoke aerosol single scattering albedo computed with relaxed constraints on the spectral variation of imaginary refractive index

As was discussed briefly in Section 2.2, the assumption regarding constraint on the spectral variation in the imaginary part of the refractive index (IPRI) is being analyzed for relaxing the strong constraint in V3 that is applied to the retrievals of fine mode dominated aerosol cases. This strong control of the spectral IPRI in V3 was applied based on the assumption that BC is the primary absorber in fine mode aerosols and also since there is some evidence that the spectral variation of IPRI for BC is very small (Kirchstetter et al., 2004). Furthermore, when AE is high then the AOD at the longer wavelengths of 870 and 1020 nm is relatively low thus providing a weak signal in those wavelengths for the retrieval of absorption information. In Version 3 the constraint on spectral variation of IPRI is assumed to vary with particle size with strong constraint for the smallest size fine mode aerosol (high AE) and weak constraint for coarse mode dominated aerosol (low AE). As outlined in Sinyuk et al. (2022), the weak constraint at low AE allows for the strong spectral variation in absorption from the mid-visible to UV wavelengths that is primarily due to absorption by iron oxide content in coarse mode mineral dust (Di Biagio et al., 2019). Also, for dust cases with low AE the AOD is relatively high at all wavelengths thereby providing sufficient signal for retrieving absorption over the entire spectral range. Additionally for retrievals that include the 380 nm wavelength an alternative calibration of the sky radiances for

that channel was applied since the integrating sphere that was used to calibrate all other wavelengths did not produce a strong enough radiance signal in the UV. Therefore the vicarious method of Li et al. (2008) was utilized to compute the instrument field of view (FOV) at 870 nm and then the assumption of constant FOV across all wavelengths was applied in order to determine sky radiances calibration at 380 nm. It is emphasized here that all of the relaxed constraint retrievals presented here are preliminary since this work is in the research phase plus the sky radiance calibration at 380 nm is also preliminary and therefore subject to change.
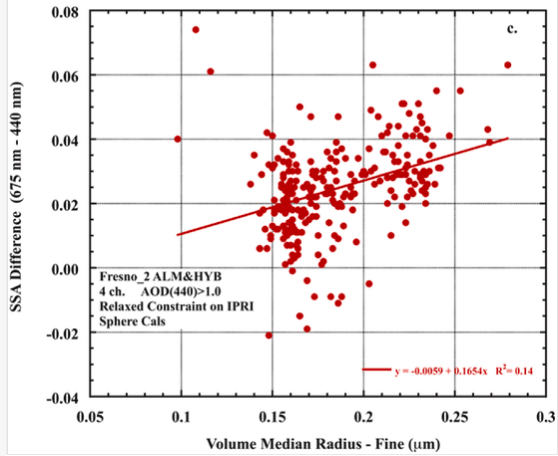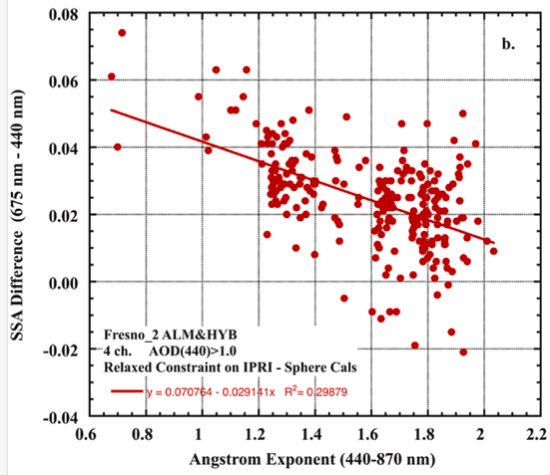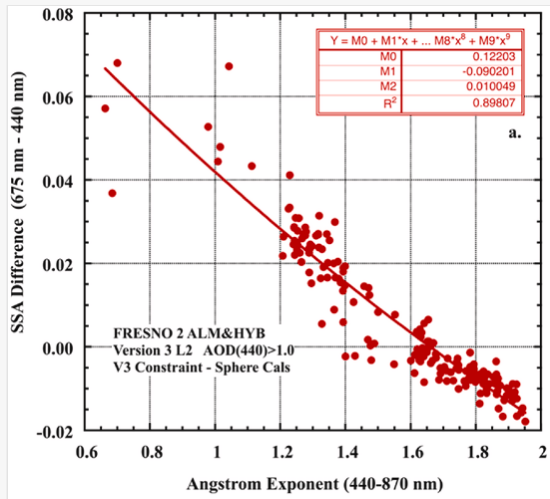
Only the constraint on IPRI was changed in the relaxed (REL) retrievals and therefore the changes in the retrieved real part of refractive index and aerosol size distributions were very small and insignificant. Sinyuk et al. (2022) showed that for fine mode dominated biomass burning cases that the retrieved volume median radius of the fine mode differed by less than 0.001 μm between the standard retrieval applied in V3 and the REL retrievals. Therefore, in this section we only focus on the change in absorption as parameterized by the single scattering albedo, for retrievals made with the REL assumption on the IPRI.

First we examine the data for the Fresno, CA site utilizing only L2 data of both almucantar and hybrid retrievals in V3 since final calibration yielding accurate sky radiances is important in the retrieval of SSA. The high AOD cases at this site result from biomass burning emissions and we focus on the cases with AOD >1.0 at 440 nm (most from 2020) which insures highly accurate retrieval of SSA. For AOD(440) = 1 for fine mode aerosols the estimated uncertainties in retrieved SSA are ∼0.015–∼0.02 at 440 nm and 675 nm, and this uncertainty decreases as AOD(440) increases to even higher levels (Sinyuk et al., 2020). Here we focus on spectral SSA difference 675 nm–440 nm since it is indicative of the magnitude of BrC and/or coated BC absorption for fine mode dominated aerosols. BrC absorption is expected to be very small at 675 nm yet significant at 440 nm (Kirchstetter et al., 2004) therefore yielding lower SSA at 440 nm when BrC absorption is relatively strong. However for particles with a BC core and a coating of organic carbon the SSA at 440 nm may also be lower than at 675 nm (Wang et al., 2016). In Fig. 15a the SSA difference 675 nm–440 nm at the Fresno site is shown as a function of AE (440–870) for the V3 data. Here in Fig. 15 the AE(440−870) is computed slightly differently using 440, 675 and 870 nm AOD (no 500 nm AOD) in linear regression since these are the coincident AOD that are input to the almucantar and hybrid inversions. In V3 the constraint on the wavelength dependence of IPRI varies as a function of AE with strong constraint on the spectral variation at high AE that gets progressively relaxed as AE decreases. This results in a highly defined and largely monotonic relationship of SSA difference as a function of AE in the V3 database, seen in Fig. 15a, with $r^2 = 0.90$ for a second order fit of the data. In the inversions with the new relaxed constraint on IPRI (Sinyuk et al., 2022) shown in Fig. 15b there is much more scatter in SSA(675-440 nm) as a function of AE (linear fit $r^2 = 0.30$) presumably due to variations in fuel type and combustion conditions, however there was still a general increase in SSA difference as AE decreases. This suggests that BrC absorption and/or absorption from coated BC in general increased as AE decreased. There are more retrievals with the new relaxed constraints than in V3 due to the often smaller sky residual errors with the relaxed constraints versus the standard constraint in V3 (Sinyuk et al., 2022). In other words, the fit of calculated to measured sky radiance data is typically better with the relaxed constraint retrievals. Spectral SSA determined from in situ surface measurements of five different forest fire smoke plumes in the western US in 2019 by Jordan et al. (2022) showed the 675-440 nm SSA difference to range from −0.015 to 0.043. This is within the range of values from the relaxed retrievals shown in Fig. 15b. AERONET retrieved SSA difference for the relaxed retrievals as a function volume median fine mode radius shows a general increase as fine mode radius increased, however with much scatter and relatively low correlation (Fig. 15c). This increase in SSA difference with increasing fine radius is nonetheless consistent with the measurements of Di Lorenzo et al. (2017, 2018) who found that the majority of BrC absorption occurred in the larger mass biomass burning molecules and larger submicron particles, and that these particles continued to absorb after aging. However, this does not rule out the possibility of the observed spectral absorption being due to coated BC completely or possibly in combination with BrC.

alt-text: Fig. 15

Fig. 15

a.

$Y = M0 + M1*x + ... M8*x^8 + M9*x^9$	
M0	0.12203
M1	-0.090201
M2	0.010049
R^2	0.89807

FRESNO 2 ALM&HYB
Version 3 L2   AOD(440)>1.0
V3 Constraint - Sphere Cals

Angstrom Exponent (440-870 nm)
SSA Difference (675 nm - 440 nm)

b.

Fresno_2 ALM&HYB
4 ch.   AOD(440)>1.0
Relaxed Constraint on IPRI - Sphere Cals

y = 0.070764 - 0.029141x R^2= 0.29879

Angstrom Exponent (440-870 nm)
SSA Difference (675 nm - 440 nm)

c.

Fresno_2 ALM&HYB
4 ch.   AOD(440)>1.0
Relaxed Constraint on IPRI
Sphere Cals

y = -0.0059 + 0.1654x R^2= 0.14

Volume Median Radius - Fine (μm)
SSA Difference (675 nm - 440 nm)

(a) Spectral SSA difference 675 nm–440 nm at the Fresno site as a function of AE (440–870) for V3 retrievals. (b) Experimental inversions with the relaxed constraint on IPRI (Sinyuk et al., 2022) showing much more scatter in spectral SSA difference (675-440 nm) as a function of AE. (c) SSA difference (675–440 nm) as a function of retrieved volume median fine mode radius showing a general increase as fine mode radius increased, however with much scatter and relatively low correlation.

The retrieval of SSA for the transported smoke case at GSFC on Sep 15, 2020 was next examined for inversions made utilizing different assumptions on the constraint of the IPRI and also the number of wavelengths of AOD and sky radiance data that were input to the algorithm (4 or 6 wavelengths). This comparison is shown in Fig. 16 for the retrievals made using the measurements from 1342 UTC, the same case shown in the previous GSFC analyses. At most wavelengths the differences are less than 0.004 for both standard and relaxed constraints on the IPRI, however at 675 there is one exception where the 4-channel relaxed inversion difference is 0.012 greater at 675 nm than the inversions made for the standard constraint retrievals for both 4 and 6 channels. These differences between standard and relaxed constraints are quite small due to the low AE (440–870 nm) of 0.67 for this case, thereby already employing a weak constraint on the spectral IPRI in the standard retrieval utilized in V3, a constraint that is similar to the REL constraint that is applied for all AE levels. Since the smoke layer for this GSFC transported smoke was at such a high altitude, the effect of the altitude of the aerosol layer on the retrieval was also investigated. The retrievals were run for the relaxed IPRI constraint case with the aerosol concentration centered at 5 km with a Gaussian distribution having a standard deviation of 0.5 km: the aerosol height for the smoke layer on this date and time was measured by the MPL lidar located at GSFC (see Fig. 8a). This was compared with the retrievals using the standard V3 aerosol profiles which were obtained for each date and location from MERRA-2 reanalysis (Sinyuk et al., 2020). The differences in SSA were found to be quite small ranging from ~0.0001 at 1020 and 870 nm to 0.0025 at 440 nm for the 4-channel retrieval. For the 6-channel retrieval the SSA differences were similar for 1020 and 870 nm and slightly higher at ~0.006 for 440 nm and 380 nm. All differences due to altitude showed slightly higher SSA for the retrievals made with the realistic aerosol height centered at 5 km, as compared to the height from MERRA-2. From this comparison we conclude that the effect on the almucantar retrievals of actual aerosol layer height versus the profile used in V3 for this extreme case of an elevated smoke layer was relatively insignificant.

ⓘ Images are optimised for fast web viewing. Click on the image to view the original version.
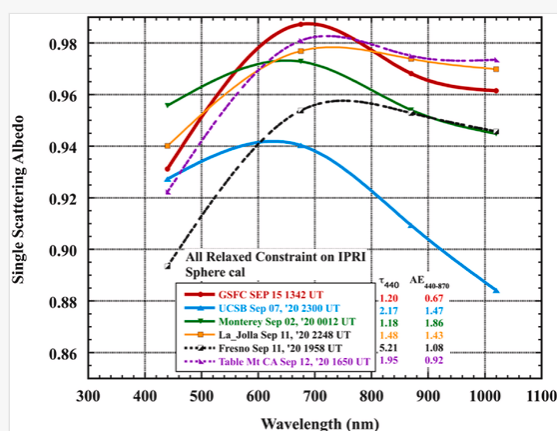
alt-text: Fig. 16

Fig. 16
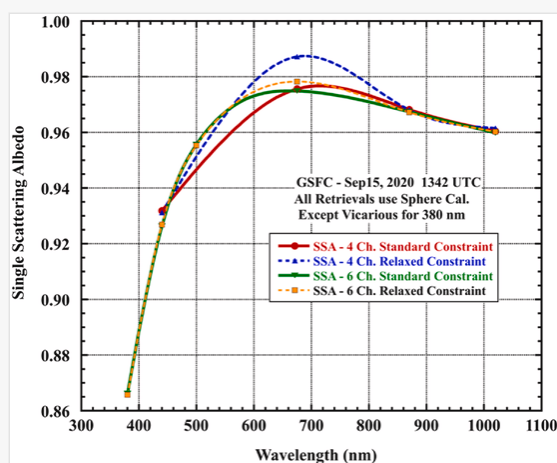
The same SSA retrievals shown in Fig. 9c for the California smoke cases in the general vicinity of major fires were also inverted with the relaxed constraint on the spectral imaginary refractive index. Fig. 17 shows spectral SSA for the standard 4-channel retrievals with the REL constraint instead of the standard constraint utilized in V3. The spectral SSA for the cases at Fresno, Table Mountain, and GSFC all showed similar strong spectral signature of 440 nm SSA much less than 675 nm with both the REL constraint and the standard V3 constraint applied to the inversions. This occurs due to the relatively low AE(440–870), ranging from 0.67 to 1.08, for these three sites/cases, thereby invoking a somewhat relaxed constraint in IPRI even in the V3 retrievals. However the three sites with high AE, ranging from 1.43 to 1.86, showed significantly lower SSA at 440 relative to 675 nm for the REL retrievals while for the standard V3 retrievals the spectral SSA differences were small. The 675-440 nm SSA difference between the two retrievals is largest for the La Jolla case where it was 0.037 for the relaxed retrieval while only 0.004 for the standard V3 retrieval. In this case at La Jolla the REL retrieval likely indicates the presence of significant BrC and/or coated BC absorption while for the V3 retrieval the shorter wavelength absorption signal is minimal since the strong constraint on spectral IPRI had damped out the spectral absorption signal. When the REL constraint is used for all retrievals as in Fig. 17 there was a signature of BrC and/or coated BC absorption for all sites but with varying magnitude of the relative absorption as parameterized by the SSA difference between 675 nm and 440 nm.

Images are optimised for fast web viewing. Click on the image to view the original version.

alt-text: Fig. 17

Fig. 17

Similar to Fig. 9c for the California smoke cases in the general vicinity of major fires, however inverted with the relaxed constraint on the spectral imaginary refractive index. Spectral SSA were retrieved for the standard 4 wavelength input with the REL constraint instead of the standard constraint utilized in V3.

Next, we compare the aerosol optical properties of some selected smoke events that had high AOD at various global locations. All of the SSA retrievals for these cases were made with the relaxed constraints on the spectral variation of the imaginary refractive index. As previously mentioned, the high AOD of these cases ensures that there is very good sensitivity and small uncertainty to the retrieved aerosol parameters (Sinyuk et al., 2020). Two of these cases included significant contributions from the burning of subsurface peat, one in central Alaska in Sep 2004 (Bonanza Creek site) and the other in Kalimantan, Indonesia in Aug 2015 (Palangkaraya site), both in or near the respective biomass burning source regions. The other cases compared were a long-distance transported smoke plume from Quebec, Canada from severe boreal forest wildfires in 2002 that was transported to the GSFC site in Maryland, plus a case of high AOD from southern African savanna burning measured in Mongu, Zambia that is located within an extensive savanna burning region. The normalized AOD spectra for these cases (Fig. 18a) show that all except the Sep 15, 2020 case at GSFC exhibited increasing AOD as wavelength decreased below 500 nm, and all also significantly steeper decreases in AOD

for $\lambda > 500$ nm as compared to the GSFC case. The comparison of the size distributions for these cases (Fig. 18b) shows that the peak fine mode radius of the GSFC case is much larger than all of the other cases. This occurred despite the particle radius for the Palangkaraya and Bonanza Creek cases being significantly larger than for most biomass burning smoke (Reid et al., 2005). The width of the fine mode volume distribution is significantly narrower for the GSFC aged smoke case in comparison to the other five cases. This is especially evident in comparison to the two peat burning cases in Alaska and Indonesia. The comparison of the spectral SSA (Fig. 18c) shows a much stronger decrease in SSA at the 440 and 380 nm wavelengths relative to 675 nm for the GSFC long-distance smoke transport case as compared to all of the other cases. In particular, the comparison of the GSFC case to the Palangkaraya case is notable since these retrievals were both done with relaxed constraints and also were both six-wavelength inversions adding the 380 nm and 500 nm data. The large decreases in SSA at the shortest wavelengths for the GSFC case strongly suggests significant BrC and/or coated BC absorption while the relatively flat SSA spectra with high SSA at 0.96 ± 0.01 from 380 to 870 nm at Palangkaraya indicates relatively weak absorption for that case. This two site comparison suggests that very different types of biomass burning produce very different magnitudes of absorption. The burning in the region surrounding Palagkaraya was dominated by smoldering combustion from peat burning which apparently resulted in relatively little BC in the aerosol (Stockwell et al., 2016) and also resulting in a relatively low altitude smoke layer. In contrast the burning of forests in the West coast US states (subsequently transported to GSFC) was at extremely high intensity with much flaming combustion which resulted in strong convective updrafts and associated vertical transport to relatively high altitudes. Studies by Saleh et al. (2014), Lu et al. (2015) and McClure et al. (2020) have all found that the imaginary refractive index of BrC decreases as the ratio of BC to organic carbon (OC) decreases. Stockwell et al. (2016) made situ measurements of spectral SSA for Indonesian peat during the same major 2015 burning season in the same region of Kalimantan. They found that the SSA at 405 nm was 0.974 versus SSA at 870 nm of 0.998, this difference in SSA of 0.024 was attributed almost entirely to BrC absorption although this spectral SSA difference is greater than the AERONET retrieval for Palangkaraya, yet substantially smaller than from the GSFC case. It is noted that the measurements made by Stockwell et al. (2016) were at ground level while the AERONET retrievals are representative of the total atmospheric column, and that some of the aerosol in the column is aged significantly which may result in differences in absorption. Aging of BrC by photolysis has been shown to weaken absorption for smoldering combustion aerosols (Sumlin et al., 2017). Therefore the smaller 440–675 nm SSA difference in the AERONET total column retrievals compared to fresh smoke at the surface as measured by Stockwell et al. (2016) may be partly due to aerosol aging. Additionally some of the smoke in the total column is not peat smoke with peat burning comprising ~80%−85% of the total biomass burning emissions from the 2015 fires in Indonesia (Kaiser et al., 2016; Wiggins et al., 2018; Eck et al., 2019). At a different site, the retrieval for the Mongu, Zambia case in Fig. 18c also includes 380 nm data and it is seen that there is only a relatively small decrease in SSA at 380 nm relative to 440 nm, which can be attributed to BrC and/or coated BC content in the aerosol. This is consistent with the more extensive analysis of multiple retrievals at high AOD at the Mongu site presented in Sinyuk et al. (2022), which also showed much smaller decreases in SSA at 380 nm versus 440 nm as compared to forest fire smoke from sites in the western USA. The small SSA decrease at 380 nm at the Mongu site is consistent with the spectral BrC absorption measured by Kirchstetter et al. (2004) for savanna burning smoke in southern Africa, however it appears that absorption by BC dominates in this savanna region with strong aerosol absorption (low SSA; Eck et al. 2003; Ward et al., 1996), especially early in the burning season (Eck et al., 2013). For this Mongu case with high BC content from savanna burning the smaller decrease in 380 nm versus 440 nm and 500 nm SSA as compared to the GSFC smoke event case may not be consistent with the findings of Saleh et al. (2014) and McClure et al. (2020) who found that the imaginary refractive index of BrC increases as the ratio of BC to organic carbon (OC) increases. However, it is possible that the actual BrC absorption is strong for the Mongu case but that there are low concentrations of BrC thereby resulting in a relatively small decreases in SSA at 440 nm and 380 nm.

(i) Images are optimised for fast web viewing. Click on the image to view the original version.

alt-text: Fig. 18

Fig. 18
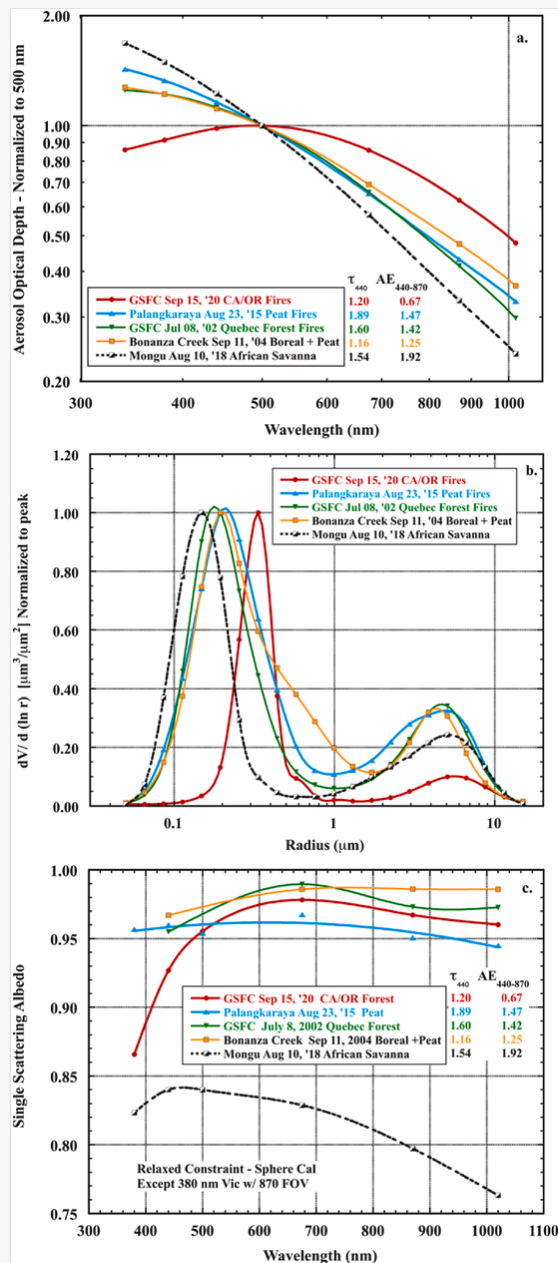
(a) Normalized AOD spectra (to 500 nm) of some selected smoke events with high AOD at various global locations, compared to the GSFC case of Sep 15, 2020. (b) Comparison of the normalized size distributions for these same cases shows that the peak fine mode radius of the GSFC case is much larger than all of the other cases, plus with significantly narrower width. (c) Comparison of the spectral SSA retrievals for these same cases. These SSA retrievals were made with the relaxed (REL) constraints on the spectral variation of the imaginary refractive index, with some utilizing 4 wavelengths while others that had advanced instruments had 6 wavelengths (380 nm and 500 nm added).

4 Summary and conclusions

The biomass burning season of August–October in 2020 in California and Oregon was exceptional in the amount of area burned (record breaking year in CA) and in the severity of the fires. Fire frequency and intensity has been increasing in this region in recent decades with expected increasing probability of additional severe burning years in the

future. Here we utilized data from several AERONET monitoring sites to investigate the measured spectra of aerosol optical depth and retrieved aerosol optical properties (size distribution and single scattering albedo) during this extreme burning season, plus comparisons to other years. Analysis of data was primarily performed for sites located close to the forest fire sources in California and for sites at varying distances from the fires in North America, including sites near the US east coast. The principal findings and conclusions of this work are summarized as follows.

1) Comparison of the 2020 burning season AOD to all other years back to 2002 for three sites in California reveal the extreme magnitude of the smoke emitted from the severe forest fires in that year. For example, at the Fresno site the number of days with very high daily averages of AOD (>1 at 440 nm) was much higher in 2020 with 24 days as compared to any other years during the monitoring record, the next highest was 11 days in 2021 and third highest was 4 days in 2018. However, wind direction and transport to these sites in California relative to the location of the fire source regions also constitutes significant factors in the interannual variability of measured AOD at any given location. Additionally, an area average time series (2000–2021) of MODIS DT & DB satellite retrieved AOD at 550 nm encompassing all of CA and OR plus adjacent areas showed the highest monthly average in September 2020 and the second highest in August 2021.

2) Smoke properties close to the fire sources in California at some sites and dates in 2020 showed larger volume median fine mode particle radius than typically measured for smoke particles. The particle radii were larger in some days in 2020 than 2021 even though both were extreme burning seasons with high intensity and numbers of wildfires, thus indicating the unusual nature of some of the smoke emitted in 2020, in addition to aging processes.

3) Fine mode smoke particle size also showed very large variability in 2020 burning season at some sites in California and throughout the US in mid-September. For example at the Monterey site on the Pacific coast the volume median particle radius varied over the range of 0.15 μm–0.32 μm for the high AOD range of 0.8–1.4 at 440 nm. This suggests large variability in combustion fuel type, combustion phases and aging of the emitted aerosols. This has implications for satellite retrievals of smoke optical properties in such dynamic conditions.

4) Retrievals at some locations and dates in California indicated strong BrC and or coated BC absorption signals (SSA 675 nm > 440 nm) in 2020 suggesting that significant absorption occurred from both BrC and BC for smoke particles in this extreme year. A new research level retrieval provided more insight into this spectral absorption occurrence and magnitude, but these results should be considered preliminary. However, for some of the smoke events even the current operational V3 retrievals showed similar strong absorption at 440 nm relative to 675 nm in 2020 compared with the research algorithm (with relaxed constraint on spectral imaginary index), due to the large particle size during these events and resulting lower Angstrom Exponent values than typical. These low AE values resulted in relaxed constraints even in the V3 retrievals.

5) Smoke optical properties of some of the long-distance transported smoke showed extreme AOD spectra and size distributions that are very rare in the 29 years of AERONET monitoring. Specifically, AOD spectra with maximum values at 500 nm were measured in the smoke plume at the GSFC site in Maryland on Sep 15, 2020. AOD spectra with maximum at 500 nm and lower values at 440 nm and the UV wavelengths are very unusual and are the result of an extreme size distribution for fine mode sized particles. The fine mode (sub-micron) size distribution for this GSFC case had very large volume median radius of 0.32 μm and also very narrow width of standard deviation 0.33 (geometric standard deviation = 1.39), both of which are extreme for smoke particles or any other atmospheric aerosol type. Mie calculations showed that the extreme size distribution was the principal reason for the associated anomalous AOD spectra.

6) In addition to the extreme size distribution retrieved at GSFC on Sep 15, 2020 the spectral single scattering albedo was ~0.04 higher at 675 nm versus 440 nm. This relatively unusual absorption spectra for smoke indicates strong absorption by BrC and/or coated BC. This is a long-distance transport aged smoke case and therefore suggests that the spectral absorption signature in this smoke plume was long-

lived at greater than ∼5 days after fire emission. This is significantly longer than BrC has typically been observed to persist in the atmosphere in most previous studies, if this spectral SSA difference were primarily due to BrC.

7) A comparison of retrievals made with a new relaxed constraint on the imaginary part of the refractive index to the standard constraints applied to the retrievals made in V3 was done for the Fresno site smoke data. Analysis focused on cases with very high AOD (>1 at 440 nm) in order to have small uncertainties in the retrieval of spectral absorption. For the new relaxed constraint inversions there was an increase in SSA difference 675-440 nm as AE decreased but with much scatter thereby suggesting that variation in BrC and/or coated BC content may be due to various factors such as fuel type, combustion conditions and aerosol aging processes. For the current V3 retrievals however there was a strong increase in SSA difference as AE decreased (with high correlation) due to the spectral constraint on the imaginary part that is applied in a linearly decreasing magnitude as AE decreases. This constraint in the V3 inversion algorithm therefore forced a strong relationship versus AE by repressing the retrieval of BrC and/or coated BC signatures at moderate to high levels of AE.

8) A comparison of biomass burning spectral single scattering albedo from a few selected high AOD cases from major burning regions around the globe showed a large range in spectral absorption signal that is in turn likely due to variation in fuel types, combustion conditions and particle aging. Spectral SSA retrievals with the new relaxed (REL) constraint on spectral variation of the imaginary part were utilized in order to provide a more robust assessment of the relative strength of BrC and/or coated BC absorption. A case of smoke from Palangkaraya, Indonesia during the major peat burning year of 2015 on Borneo indicated relatively weak absorption (almost spectrally flat SSA at ∼0.95–0.96) even at 380 nm. For a case of southern African savanna smoke (Mongu, Zambia) the spectral SSA were very low at 0.74 to 0.84 as is typical for this region due to significant flaming phase combustion of grass fuels (Ward et al., 1996) especially early in the burning season. The spectral absorption signature possibly due to BrC and/or coated BC for this savanna smoke case is evident in a decrease in SSA at 380 nm relative to 440 nm but the decrease was relatively modest at ∼0.017. Therefore in this savanna burning region BC dominates the absorption and the BrC signal may possibly be significant only in the UV. Two cases of high AOD boreal fire smoke were selected due to the large size of the fine mode smoke particles for these events. Both showed a moderate spectral absorption signal with SSA difference (675 nm–440 nm) of ∼0.02 (Quebec smoke case) and 0.035 (Alaska smoke case), however 380 nm sky radiance data were not measured for these two cases therefore no 380 nm SSA was retrieved.

These extreme forest fire events in the western US which occurred in 2020 encompass some atypical biomass burning aerosol properties that can potentially be further studied by utilizing simulations of aerosol aging processes. Additionally these particular events provide a challenging test for satellite retrieval of AOD and SSA due to the very high AOD levels, large variability in particle size including extremely large radii for some plumes plus a much different spectral variation in absorption than is often assumed is some retrievals.

Author statement

T.F. Eck: Conceptualization, Formal analysis, Investigation, Writing - original draft, Writing -revised draft, Visualization. **B.N. Holben:** Project administration. **J.S. Reid:** Formal analysis, Investigation, Writing - original draft, Visualization. **A. Sinyuk:** Investigation, Formal analysis. **D.M. Giles:** Validation, Formal analysis, Writing - review & editing. **Anti Arola:** Formal analysis, Investigation, Visualization **I. Slutsker:** Investigation., **J.S Schafer:** Investigation., **M. Sorokin:** Investigation. **A. Smirnov:** Investigation. **A.D. LaRosa:** Investigation. **J. Kraft:** Investigation. **E.A. Reid:** Investigation. **Norman T. O'Neill:** Investigation, Writing – revised draft. **E. J. Welton:** Data curation, Writing - original draft. **Arsenio R. Menendez:** Investigation.

Declaration of competing interest

The authors declare that they have no known competing financial interests or personal relationships that could have appeared to influence the work reported in this paper.

Acknowledgements

References

(i) The corrections made in this section will be reviewed and approved by a journal production editor. The newly added/removed references and its citations will be reordered and rearranged by the production team.

Abatzoglou, John T., Park Williams, A., 2016. Impact of anthropogenic climate change on wildfire across western US forests. Proc. Natl. Acad. Sci. USA 113 (42), 11770–11775.

Aguilera, R., Corringham, T., Gershunov, A., Benmarhnia, T., 2021. Wildfire smoke impacts respiratory health more than fine particles from other sources: observational evidence from Southern California. Nat. Commun. 12 (1), 1–8.

Barreto, Á., Cuevas, E., Granados-Muñoz, M.J., Alados-Arboledas, L., Romero, P.M., Gröbner, J., Kouremeti, N., Almansa, A.F., Stone, T., Toledano, C., Román, R., 2016. The new sun-sky-lunar Cimel CE318-T multiband photometer–a comprehensive performance evaluation. Atmos. Meas. Tech. 9 (2), 631–654.

Bond, T.C., Doherty, S.J., Fahey, D.W., Forster, P.M., Berntsen, T., DeAngelo, B.J., Flanner, M.G., Ghan, S., Kärcher, B., Koch, D., Kinne, S., 2013. Bounding the role of black carbon in the climate system: a scientific assessment. J. Geophys. Res. Atmos. 118 (11), 5380–5552.

Campbell, J.R.J.R., Hlavka, D.L., Welton, E.J., Flynn, C.J., Turner, D.D., Spinhirne, J.D., Scott, V.S., Hwang, I.H., 2002. Full-time, eye-safe cloud and aerosol lidar observation at atmospheric radiation measurement program sites: instrument and data processing. J. Atmos. Ocean. Technol. 19, 431–442.

Chen, Q., Chen, Q., Hua, X., Guan, D., Chang, T., 2021. Gas-phase brown carbon: absorbance and chromophore types. Atmos. Environ. 264, 118646.

Clarke, A.D., Howell, S., Quinn, P.K., Bates, T.S., Ogren, J.A., Andrews, E., Jefferson, A., Massling, A., Mayol-Bracero, O., Maring, H., Savoie, D., 2002. INDOEX aerosol: a comparison and summary of chemical, microphysical, and optical properties observed from land, ship, and aircraft. J. Geophys. Res. Atmos. 107 (D19), INX2-32.

Colarco, P.R., Schoeberl, M.R., Doddridge, B.G., Marufu, L.T., Torres, O., Welton, E.J., 2004. Transport of smoke from Canadian forest fires to the surface near Washington, DC: injection height, entrainment, and optical properties. J. Geophys. Res. Atmos. 109 (D6).

Di Biagio, C., Formenti, P., Balkanski, Y., Caponi, L., Cazaunau, M., Pangui, E., Journet, E., Nowak, S., Andreae, M.O., Kandler, K., Saeed, T., 2019. Complex refractive indices and single-scattering albedo of global dust aerosols in the shortwave spectrum and relationship to size and iron content. Atmos. Chem. Phys. 19 (24), 15503–15531.

Di Lorenzo, R.A., Washenfelder, R.A., Attwood, A.R., Guo, H., Xu, L., Ng, N.L., Weber, R.J., Baumann, K., Edgerton, E., Young, C.J., 2017. Molecular-size-separated brown carbon absorption for biomass-burning aerosol at multiple field sites. Environ. Sci. Technol. 51 (6), 3128–3137.

Di Lorenzo, R.A., Place, B.K., VandenBoer, T.C., Young, C.J., 2018. Composition of size-resolved aged boreal fire aerosols: brown carbon, biomass burning tracers, and reduced nitrogen. ACS Earth and Space

Chemistry 2 (3), 278–285.

Dominici, F., Peng, R.D., Bell, M.L., Pham, L., McDermott, A., Zeger, S.L., Samet, J.M., 2006. Fine particulate air pollution and hospital admission for cardiovascular and respiratory diseases. JAMA, J. Am. Med. Assoc. 295 (10), 1127–1134. doi:10.1001/jama.295.10.1127.

Dubovik, O., King, M.D., 2000. A flexible inversion algorithm for the retrieval of aerosol optical properties from Sun and sky radiance measurements. J. Geophys. Res. 105 (20), 696 673– 20.

Dubovik, O., Holben, B.N., Eck, T.F., Smirnov, A., Kaufman, Y.J., King, M.D., Tanre, D., Slutsker, I., 2002. Variability of absorption and optical properties of key aerosol types observed in worldwide locations. J. Atmos. Sci. 59, 590–608.

Dubovik, O., Smirnov, A., Holben, B.N., King, M.D., Kaufman, Y.J., Eck, T.F., Slutsker, I., 2000. Accuracy assessments of aerosol optical properties retrieved from AERONET Sun and sky-radiance measurements. J. Geophys. Res. 105, 9791–9806.

Dubovik, O., Sinyuk, A., Lapyonok, T., Holben, B.N., Mishchenko, M., Yang, P., Eck, T.F., Volten, H., Mu~noz, O., Veihelmann, B., van der Zande, W.J., Leon, J.-F., Sorokin, M., Slutsker, I., 2006. The application of spheroid models to account for aerosol particle nonsphericity in remote sensing of desert dust. J. Geophys. Res. 111, D11208. doi:10.1029/2005JD006619.

Eck, T.F., Holben, B.N., Reid, J.S., Dubovik, O., Smirnov, A., O'Neill, N.T., Slutsker, I., Kinne, S., 1999. Wavelength dependence of the optical depth of biomass burning, urban, and desert dust aerosols. J. Geophys. Res. 104 (D24), 31 333–31,349.

Eck, T.F., Holben, B.N., Reid, J.S., Sinyuk, A., Hyer, E.J., O'Neill, N.T., et al., 2009. Optical properties of boreal region biomass burning aerosols in central Alaska and seasonal variation of aerosol optical depth at an Arctic coastal site. J. Geophys. Res. 114, D11201. doi:10.1029/2008JD010870.

Eck, T.F., Holben, B.N., Sinyuk, A., Pinker, R.T., Goloub, P., Chen, H., Chatenet, B., Li, Z., Singh, R.P., Tripathi, S.N., Reid, J.S., Giles, D.M., Dubovik, O., O'Neill, N.T., Smirnov, A., Wang, P., Xia, X., 2010. Climatological aspects of the optical properties of fine/coarse mode aerosol mixtures. J. Geophys. Res. 115, D19205. doi:10.1029/2010JD014002.

Eck, T.F., et al., 2012. Fog- and cloud-induced aerosol modification observed by the Aerosol Robotic Network (AERONET). J. Geophys. Res. 117, D07206. doi:10.1029/2011JD016839.

Eck, T.F., Holben, B.N., Reid, J.S., Mukelabai, M.M., Piketh, S.J., Torres, O., Jethva, H.T., Hyer, E.J., Ward, D.E., Dubovik, O., Sinyuk, A., 2013. A seasonal trend of single scattering albedo in southern African biomass-burning particles: implications for satellite products and estimates of emissions for the world's largest biomass-burning source. J. Geophys. Res. Atmos. 118 (12), 6414–6432.

Eck, T.F., Holben, B.N., Reid, J.S., Arola, A., Ferrare, R.A., Hostetler, C.A., Crumeyrolle, S.N., Berkoff, T.A., Welton, E.J., Lolli, S., Lyapustin, A., Wang, Y., Schafer, J.S., Giles, D.M., Anderson, B.E., Thornhill, K.L., Minnis, P., Pickering, K.E., Loughner, C.P., Smirnov, A., Sinyuk, A., 2014. Observations of rapid aerosol optical depth enhancements in the vicinity of polluted cumulus clouds. Atmos. Chem. Phys. 14, 11633–11656. doi:10.5194/acp-14-11633-2014.

Eck, T.F., Holben, B.N., Giles, D.M., Slutsker, I., Sinyuk, A., Schafer, J.S., et al., 2019. AERONET remotely sensed measurements and retrievals of biomass burning aerosol optical properties during the 2015 Indonesian burning season. J. Geophys. Res. Atmos. 124. doi:10.1029/2018JD030182.

Ehlers, K., Chakrabarty, R., Moosmüller, H., 2014. Blue moons and Martian sunsets. Appl. Opt. 53 (9), 1808–1819.

Fiebig, M., Stohl, A., Wendisch, M., Eckhardt, S., Petzold, A., 2003. Dependence of solar radiative forcing of forest fire aerosol on ageing and state of mixture. Atmos. Chem. Phys. 3 (3), 881–891.

Franzi, L.M., Bratt, J.M., Williams, K.M., Last, J.A., 2011. Why is particulate matter produced by wildfires toxic to lung macrophages? Toxicol. Appl. Pharmacol. 257 (2), 182–188.

Fleming, L.T., Lin, P., Roberts, J.M., Selimovic, V., Yokelson, R., Laskin, J., Laskin, A., Nizkorodov, S.A., 2020. Molecular composition and photochemical lifetimes of brown carbon chromophores in biomass burning organic aerosol. Atmos. Chem. Phys. 20 (2), 1105–1129.

Giles, D.M., Holben, B.N., Eck, T.F., Sinyuk, A., Smirnov, A., Slutsker, I., et al., 2012. An analysis of AERONET aerosol absorption properties and classifications representative of aerosol source regions. J. Geophys. Res. 117, D17203. doi:10.1029/2012JD018127.

Giles, D.M., Sinyuk, A., Sorokin, M.G., Schafer, J.S., Smirnov, A., Slutsker, I., et al., 2019. Advancements in the Aerosol Robotic Network (AERONET) Version 3 database—automated near-real-time quality control algorithm with improved cloud screening for Sun photometer aerosol optical depth (AOD) measurements. Atmos. Meas. Tech. 12, 169–209. doi:10.5194/amt-12-169-2019.

Goss, M., Swain, D.L., Abatzoglou, J.T., Sarhadi, A., Kolden, C.A., Williams, A.P., Diffenbaugh, N.S., 2020. Climate change is increasing the likelihood of extreme autumn wildfire conditions across California. Environ. Res. Lett. 15 (9), 094016.

Griffin, D., McLinden, C.A., Dammers, E., Adams, C., Stockwell, C.E., Warneke, C., Bourgeois, I., Peischl, J., Ryerson, T.B., Zarzana, K.J., Rowe, J.P., Volkamer, R., Knote, C., Kille, N., Koenig, T.K., Lee, C.F., Rollins, D., Rickly, P.S., Chen, J., Fehr, L., Bourassa, A., Degenstein, D., Hayden, K., Mihele, C., Wren, S.N., Liggio, J., Akingunola, A., Makar, P., 2021. Biomass burning nitrogen dioxide emissions derived from space with TROPOMI: methodology and validation. Atmos. Meas. Tech. 14, 7929–7957. doi:10.5194/amt-14-7929-2021.

Gumber, A., Reid, J.S., Holz, R.E., Eck, T.F., Hsu, N.C., Levy, R.C., Zhang, J., Veglio, P., 2022. Assessment of severe aerosol events from NASA MODIS and VIIRS aerosol products for data assimilation and climate continuity. Atmos. Meas. Tech. Discuss. [preprint] submitted for publication doi:10.5194/amt-2022-290.

Heo, J., Schauer, J.J., Yi, O., Paek, D., Kim, H., Yid, S.-M., 2014. Fine particle air pollution and mortality importance of specific sources and chemical species. Epidemiology 25 (3). doi:10.1097/EDE.0000000000000044. ISSN: 1044-3983/14/2503-0379.

Hodshire, A.L., Bian, Q., Ramnarine, E., Lonsdale, C.R., Alvarado, M.J., Kreidenweis, S.M., Jathar, S.H., Pierce, J.R., 2019. More than emissions and chemistry: fire size, dilution, and background aerosol also greatly influence near-field biomass burning aerosol aging. J. Geophys. Res. Atmos. 124 (10), 5589–5611.

Hogan, T.F., Liu, M., Ridout, J.A., et al., 2014. The Navy global environmental model. Oceanography 27, 116–125. https://www.jstor.org/stable/24862194.

Holben, B.N., Eck, T.F., Slutsker, I., Smirnov, A., Sinyuk, A., Schafer, J., et al., 2006. AERONET's version 2.0 quality assurance criteria. Remote Sensing of Atmosphere and Clouds. Proc. SPIE-Int. Soc. Opt. Eng. 6408, 64080Q. doi:10.1117/12.706524.

Holben, B.N., Eck, T.F., Slutsker, I., Tanre, D., Buis, J.P., Setzer, A., et al., 1998. AERONET—a federated instrument network and data archive for aerosol characterization. Rem. Sens. Environ. 66 (1), 1–16. doi:10.1016/S0034-4257(98)00031-5.

Higuera, P.E., Abatzoglou, J.T., 2021. Record-setting climate enabled the extraordinary 2020 fire season in the western United States. Global Change Biol. 27 (1).

Iglesias, V., Balch, J.K., Travis, W.R., 2022. US fires became larger, more frequent, and more widespread in the 2000s. Sci. Adv. 8 (11), eabc0020.

Johnson, B.T., Osborne, S.R., 2011. Physical and optical properties of mineral dust aerosol measured by aircraft during the GERBILS campaign. Q. J. R. Meteorol. Soc. 137 (658), 1117–1130. doi:10.1002/qj.777.

Jones, G.M., Gutiérrez, R.J., Tempel, D.J., Whitmore, S.A., Berigan, W.J., Peery, M.Z., 2016. Megafires: an emerging threat to old-forest species. Front. Ecol. Environ. 14 (6), 300–306.

Jordan, C.E., Anderson, B.E., Barrick, J.D., Blum, D., Brunke, K., Chai, J., et al., 2022. Beyond the ångström exponent: probing additional information in spectral curvature and variability of in situ aerosol hyperspectral (0.3-0.7 μm) optical properties. J. Geophys. Res. Atmos. 127, e2022JD037201. doi:10.1029/2022JD037201.

Kaiser, J.W., van der Werf, G.R., Heil, A., 2016. Global climate biomass burning in "State of the climate in 2015.". Bull. Am. Meteorol. Soc. 97 (8), S1–S275. doi:10.1175/2016BAMSStateoftheClimate.1.

King, M.D., Menzel, W.P., Kaufman, Y.J., Tanré, D., Gao, B.C., Platnick, S., Ackerman, S.A., Remer, L.A., Pincus, R., Hubanks, P.A., 2003. Cloud and aerosol properties, precipitable water, and profiles of temperature and water vapor from MODIS. IEEE Trans. Geosci. Rem. Sens. 41 (2), 442–458.

Kirchstetter, T.W., Novakov, T., Hobbs, P.V., 2004. Evidence that the spectral dependence of light absorption by aerosols is affected by organic carbon. J. Geophys. Res. Atmos. 109 (D21).

Konovalov, I.B., Golovushkin, N.A., Beekmann, M., Panchenko, M.V., Andreae, M.O., 2021. Inferring the absorption properties of organic aerosol in Siberian biomass burning plumes from remote optical observations. Atmos. Meas. Tech. 14, 6647–6673. doi:10.5194/amt-14-6647-2021.

Konovalov, I.B., Golovushkin, N.A., Beekmann, M., Turquety, S., 2022. Using multi-platform satellite observations to study the atmospheric evolution of Brown carbon in siberian biomass burning plumes. Rem. Sens. 14, 2625. doi:10.3390/rs14112625.

Larrabee, W.H., 1884. Green suns and red sunsets. Popular Science Monthly 24, 598–603.

Leahy, L.V., Anderson, T.L., Eck, T.F., Bergstrom, R.W., 2007. A synthesis of single scattering albedo of biomass burning aerosol over southern Africa during SAFARI 2000. Geophys. Res. Lett. 34, L12814. doi:10.1029/2007GL029697.

Levy, R.C., Mattoo, S., Munchak, L.A., Remer, L.A., Sayer, A.M., Patadia, F., Hsu, N.C., 2013. The Collection 6 MODIS aerosol products over land and ocean. Atmos. Meas. Tech. 6, 2989–3034. doi:10.5194/amt-6-2989-2013.

Lewis, K., Arnott, W.P., Moosmuller, H., Wold, C.E., 2008. Strong spectral variation of biomass smoke light absorption and single scattering albedo observed with a novel dual-wavelength photoacoustic instrument. J. Geophys. Res. 113, D16203. doi:10.1029/2007JD009699.

Li, Z., Blarel, L., Podvin, T., Goloub, P., Buis, J.P., Morel, J.P., 2008. Transferring the calibration of direct solar irradiance to diffuse-sky radiance measurements for CIMEL Sun-sky radiometers. Appl. Opt. 47 (10), 1368–1377.

Lu, Z., Streets, D.G., Winijkul, E., Yan, F., Chen, Y., Bond, T.C., Feng, Y., Dubey, M.K., Liu, S., Pinto, J.P., Carmichael, G.R., 2015. Light absorption properties and radiative effects of primary organic aerosol emissions. Environ. Sci. Technol. 49 (8), 4868–4877.

Luković, J., Chiang, J.C.H., Blagojević, D., Sekulić, A., 2021. A later onset of the rainy season in California. Geophys. Res. Lett. 48, e2020GL090350. doi:10.1029/2020GL090350.

McClure, C.D., Lim, C.Y., Hagan, D.H., Kroll, J.H., Cappa, C.D., 2020. Biomass-burning-derived particles from a wide variety of fuels–Part 1: properties of primary particles. Atmos. Chem. Phys. 20 (3), 1531–1547.

Mok, J., Krotkov, N.A., Arola, A., Torres, O., Jethva, H., Andrade, M., Labow, G., Eck, T.F., Li, Z., Dickerson, R.R., Stenchikov, G.L., 2016. Impacts of brown carbon from biomass burning on surface UV and ozone photochemistry in the Amazon Basin. Sci. Rep. 6 (1), 1–9.

O'Neill, N.T., Eck, T.F., Holben, B.N., Smirnov, A., Royer, A., Li, Z., 2002. Optical properties of boreal forest fire smoke derived from Sun photometry. J. Geophys. Res. Atmos. 107 (D11) AAC-6.

O'Neill, N.T., Thulasiraman, S., Eck, T.F., Reid, J.S., 2005. Robust optical features of fine mode size distributions: application to the Québec smoke event of 2002. J. Geophys. Res. 110, D11207. doi:10.1029/2004JD005157.

Parks, S.A., Abatzoglou, J.T., 2020. Warmer and drier fire seasons contribute to increases in area burned at high severity in western US forests from 1985 to 2017. Geophys. Res. Lett. 47, e2020GL089858. doi:10.1029/2020GL089858.

Pokhrel, R.P., Wagner, N.L., Langridge, J.M., Lack, D.A., Jayarathne, T., Stone, E.A., Stockwell, C.E., Yokelson, R.J., Murphy, S.M., 2016. Parameterization of single-scattering albedo (SSA) and absorption Ångström exponent (AAE) with EC/OC for aerosol emissions from biomass burning. Atmos. Chem. Phys. 16 (15), 9549–9561.

Pokhrel, R.P., Beamesderfer, E.R., Wagner, N.L., Langridge, J.M., Lack, D.A., Jayarathne, T., Stone, E.A., Stockwell, C.E., Yokelson, R.J., Murphy, S.M., 2017. Relative importance of black carbon, brown carbon, and absorption enhancement from clear coatings in biomass burning emissions. Atmos. Chem. Phys. 17, 5063–5078. doi:10.5194/acp-17-5063-2017.

Pueschel, R.F., Russell, P.B., Allen, D.A., Ferry, G.V., Snetsinger, K.G., Livingston, J.M., Verma, S., 1994. Physical and optical properties of the Pinatubo volcanic aerosol: aircraft observations with impactors and a Sun-tracking photometer. J. Geophys. Res. 99 (D6), 12 915–12,922 doi:10.1029/94JD00621.

Reid, C.E., Brauer, M., Johnston, F.H., Jerrett, M., Balmes, J.R., Elliott, C.T., 2016. Critical review of health impacts of wildfire smoke exposure. Environ. Health Perspect. 124 (9), 1334–1343.

Reid, J.S., Eck, T.F., Christopher, S.A., Hobbs, P.V., Holben, B.N., 1999. Use of the Ångstrom exponent to estimate the variability of optical and physical properties of aging smoke particles in Brazil. J. Geophys. Res. 104 (27), 489 473–27.

Reid, J.S., Koppmann, R., Eck, T., Eleuterio, D., 2005. A review of biomass burning emissions part II: intensive physical properties of biomass burning particles. Atmos. Chem. Phys. 5, 799–825 SRef-ID: 1680-7324/acp/2005-5-799 http://www.atmos-chem-phys.org/acp/5/799/.

Reid, J.S., Brooks, B., Crahan, K.K., Hegg, D.A., Eck, T.F., O'Neill, N., et al., 2006. Reconciliation of coarse mode sea-salt aerosol particle size measurements and parameterizations at a subtropical ocean receptor site. J. Geophys. Res. 111 (D2), D02202. doi:10.1029/2005JD006200.

Reid, J.S., Reid, E.A., Walker, A., Piketh, S., Cliff, S., Al Mandoos, A., et al., 2008. Dynamics of southwest Asian dust particle size characteristics with implications for global dust research. J. Geophys. Res. 113, D14212. doi:10.1029/2007JD009752.

Saleh, R., Robinson, E.S., Tkacik, D.S., Ahern, A.T., Liu, S., Aiken, A.C., Sullivan, R.C., Presto, A.A., Dubey, M.K., Yokelson, R.J., Donahue, N.M., 2014. Brownness of organics in aerosols from biomass burning linked to their black carbon content. Nat. Geosci. 7 (9), 647–650.

Sayer, A.M., Munchak, L.A., Hsu, N.C., Levy, R.C., Bettenhausen, C., Jeong, M.J., 2014. MODIS Collection 6 aerosol products: comparison between Aqua's e-Deep Blue, Dark Target, and "merged" data sets, and usage recommendations. J. Geophys. Res. Atmos. 119 (24), 13–965.

Sand, M., Samset, B.H., Myhre, G., Gliß, J., Bauer, S.E., Bian, H., Chin, M., Checa-Garcia, R., Ginoux, P., Kipling, Z., Kirkevåg, A., 2021. Aerosol absorption in global models from AeroCom phase III. Atmos. Chem. Phys. 21 (20), 15929–15947.

Schafer, J.S., Eck, T.F., Holben, B.N., Artaxo, P., Duarte, A.F., 2008. Characterization of the optical properties of atmospheric aerosols in Amazônia from long-term AERONET monitoring (1993–1995 and 1999–2006). J. Geophys. Res. 113, D04204. doi:10.1029/2007JD009319.

Schafer, J.S., Eck, T.F., Holben, B.N., Thornhill, K.L., Anderson, B.E., Sinyuk, A., et al., 2014. Intercomparison of aerosol single scattering albedo derived from AERONET surface radiometers and LARGE in situ aircraft profiles during the 2011 DRAGON-MD and DISCOVER-AQ experiments. J. Geophys. Res. Atmos. 119, 7439–7452. doi:10.1002/2013JD021166.

Schafer, J.S., Eck, T.F., Holben, B.N., Thornhill, K.L., Ziemba, L.D., Sawamura, P., Moore, R.H., Slutsker, I., Anderson, B.E., Sinyuk, A., Giles, D.M., Smirnov, A., Beyersdorf, A.J., Winstead, E.L., 2019. Intercomparison of aerosol volume size distributions derived from AERONET ground-based remote sensing and LARGE in situ aircraft profiles during the 2011-2014 DRAGON and DISCOVER-AQ experiments. Atmos. Meas. Tech. 12, 5289–5301. doi:10.5194/amt- 12-5289-2019.

Schmid, B., Michalsky, J., Halthore, R., Beauharnois, M., Harrison, L., Livingston, J., et al., 1999. Comparison of aerosol optical depth from four solar radiometers during the fall 1997 ARM intensive observation period. Geophys. Res. Lett. 26 (17), 2725–2728. doi:10.1029/1999GL900513.

Shaw, G.E., 1983. Sun photometry. Bull. Am. Meteorol. Soc. 64 (1), 4–10.

Shi, Y.R., Levy, R.C., Eck, T.F., Fisher, B., Mattoo, S., Remer, L.A., Slutsker, I., Zhang, J., 2019. Characterizing the 2015 Indonesia fire event using modified MODIS aerosol retrievals. Atmos. Chem. Phys. 19, 259–274. doi:10.5194/acp-19-259-2019.

Shi, Y.R., Levy, R.C., Yang, L., Remer, L.A., Mattoo, S., Dubovik, O., 2021. A Dark Target research aerosol algorithm for MODIS observations over eastern China: increasing coverage while maintaining accuracy at high aerosol loading. Atmos. Meas. Tech. 14, 3449–3468. doi:10.5194/amt-14-3449-2021.

Shive, K.L., Wuenschel, A., Hardlund, L.J., Morris, S., Meyer, M.D., Hood, S.M., 2022. Ancient trees and modern wildfires: declining resilience to wildfire in the highly fire-adapted giant sequoia. For. Ecol. Manag. 511, 120110.

Sinyuk, A., Holben, B.N., Smirnov, A., Eck, T.F., Slutsker, I., Schafer, J.S., et al., 2012. Assessment of error in aerosol optical depth measured by AERONET due to aerosol forward scattering. Geophys. Res. Lett. 39, L23806. doi:10.1029/2012GL053894.

Sinyuk, A., Holben, B.N., Eck, T.F., Giles, D.M., Slutsker, I., Korkin, S., Schafer, J.S., Smirnov, A., Sorokin, M., Lyapustin, A., 2020. The AERONET Version 3 aerosol retrieval algorithm, associated uncertainties and comparisons to Version 2. Atmos. Meas. Tech. 13, 3375–3411. doi:10.5194/amt-13-3375-2020.

Sinyuk, A., Holben, B., Eck, T., Giles, D., Slutsker, I., Dubovik, O., Schafer, J., Smirnov, A., Sorokin, M., 2022. Employing relaxed smoothness constraints on imaginary part of refractive index in AERONET aerosol retrieval algorithm. Atmos. Meas. Tech. Discuss. [preprint] (submitted for publication) doi:10.5194/amt-2022-60.

Smirnov, A., Holben, B.N., Dubovik, O., Frouin, R., Eck, T.F., Slutsker, I., 2003. Maritime component in aerosol optical models derived from Aerosol Robotic Network data. J. Geophys. Res. 108 (D1), 4033. doi:10.1029/2002JD002701.

Stein, A.F., Draxler, R.R., Rolph, G.D., Stunder, B.J., Cohen, M.D., Ngan, F., 2015. NOAA's HYSPLIT atmospheric transport and dispersion modeling system. Bull. Am. Meteorol. Soc. 96 (12), 2059–2077.

Stephenson, N., Brigham, C., Cag, S., Caprio, C.A., Flickinger, J., Hardlund, L., Hart, R., Hardwick, P., Mutch, L., Inventory, S.N., Shive, K., 2021. Preliminary Estimates of Sequoia Mortality in the 2020 Castle Fire. National Park Service report.

Stockwell, C.E., Jayarathne, T., Cochrane, M.A., Ryan, K.C., Putra, E.I., Saharjo, B.H., Nurhayati, A.D., Albar, I., Blake, D.R., Simpson, I.J., Stone, E.A., 2016. Field measurements of trace gases and aerosols emitted by peat fires in Central Kalimantan, Indonesia, during the 2015 El Niño. Atmos. Chem. Phys. 16 (18), 11711–11732.

Sumlin, B.J., Pandey, A., Walker, M.J., Pattison, R.S., Williams, B.J., Chakrabarty, R.K., 2017. Atmospheric photooxidation diminishes light absorption by primary brown carbon aerosol from biomass burning. Environ. Sci. Technol. Lett. 4 (12), 540–545.

Swain, D.L., 2021. A shorter, sharper rainy season amplifies California wildfire risk. Geophys. Res. Lett. 48 (5) e2021GL092843.

Turquety, S., Logan, J.A., Jacob, D.J., Hudman, R.C., Leung, F.Y., Heald, C.L., et al., 2007. Inventory of boreal fire emissions for North America in 2004: importance of peat burning and pyroconvective injection. J. Geophys. Res. 112 (D12), D12S03. doi:10.1029/2006JD007281.

Wang, X., Heald, C.L., Sedlacek, A.J., de Sá, S.S., Martin, S.T., Alexander, M.L., Watson, T.B., Aiken, A.C., Springston, S.R., Artaxo, P., 2016. Deriving brown carbon from multiwavelength absorption measurements: method and application to AERONET and Aethalometer observations. Atmos. Chem. Phys. 16 (19), 12733–12752.

Ward, D.E., Hao, W.M., Susott, R.A., Babbitt, R.E., Shea, R.W., Kaufman, J.B., Justice, C.O., 1996. Effect of fuel composition on combustion efficiency and emission factors for African savanna ecosystems. J. Geophys. Res. 101, 23569–23576.

Wegesser, T.C., Pinkerton, K.E., Last, J.A., 2009. California wildfires of 2008: coarse and fine particulate matter toxicity. Environ. Health Perspect. 117 (6), 893–897.

Welton, E.J., Campbell, J.R., Spinhirne, J.D., Scott, V.S., 2001. Global monitoring of clouds and aerosols using a network of micro-pulse lidar systems. Proc. SPIE 4153, 151–158.

Westerling, A.L., Hidalgo, H.G., Cayan, D.R., Swetnam, T.W., 2006. Warming and earlier spring increase western US forest wildfire activity. Science 313 (5789), 940–943.

Wiggins, E.B., Czimczik, C.I., Santos, G.M., Chen, Y., Xu, X., Holden, S.R., et al., 2018. Smoke radiocarbon measurements from Indonesian fires provide evidence for burning of millennia-aged peat. Proc. Natl. Acad. Sci. USA 115 (49), 12 419–12,424 doi:10.1073/pnas.1806003115.

Wilson, R., 1951. The blue sun of 1950 September. Mon. Not. Roy. Astron. Soc. 111 (5), 478–489.

Wong, J.P., Nenes, A., Weber, R.J., 2017. Changes in light absorptivity of molecular weight separated brown carbon due to photolytic aging. Environ. Sci. Technol. 51 (15), 8414–8421.

Wong, J.P., Tsagkaraki, M., Tsiodra, I., Mihalopoulos, N., Violaki, K., Kanakidou, M., Sciare, J., Nenes, A., Weber, R.J., 2019. Atmospheric evolution of molecular-weight-separated brown carbon from biomass burning. Atmos. Chem. Phys. 19 (11), 7319–7334.

Wullenweber, N., Lange, A., Rozanov, A., von Savigny, C., 2021. On the phenomenon of the blue sun. Clim. Past 17, 969–983. doi:10.5194/cp-17-969-2021.

Yang, D., Yang, A., Yang, J., Xu, R., Qiu, H., 2021. Unprecedented migratory bird die-off: a citizen-based analysis on the spatiotemporal patterns of mass mortality events in the western United States. GeoHealth 5 (4) e2021GH000395.

Zhou, X., Josey, K., Kamareddine, L., Caine, M.C., Liu, T., Mickley, L.J., Cooper, M., Dominici, F., 2021. Excess of COVID-19 cases and deaths due to fine particulate matter exposure during the 2020 wildfires in the United States. Sci. Adv. 7 (33), eabi8789.

Highlights

- AOD from forest fire smoke in the western US was exceptionally high in 2020.
- Some smoke had very large volume radius (>0.30 mm) and narrow fine width.
- These extreme size distributions resulted in maximum AOD at 500 nm in some cases.
- Large SSA differences (675-440 nm) indicated strong brown carbon absorption.
- These smoke SSA differences remained large even after 4–5 days transport and aging.

Queries and Answers

Q1

Query: Correctly acknowledging the primary **funders and grant IDs** of your research is important to ensure compliance with funder policies. Please make sure that funders are mentioned accordingly.

Answer: